Ore Geology Reviews 111 (2019) 102999

Contents lists available at ScienceDirect

Ore Geology Reviews

journal homepage: www.elsevier.com/locate/oregeorev

Characterization of ore-forming fluids in the Tamusu sandstone-type uranium deposit, Bayingobi Basin, China: Constraints from trace elements, fluid inclusions and C–O–S isotopes

Chengyong Zhang[a,b,*], Fengjun Nie[b], Yangquan Jiao[a], Wei Deng[b], Yunbiao Peng[c], Shuren Hou[c], Mingjian Dai[a,c], Tengfei Ye[b]

[a] Faculty of Earth Resource, China University of Geosciences, 430074 Wuhan, China
[b] Key Laboratory on Nuclear Resources and Environment, East China University of Technology, Nanchang, Jiangxi 330013, China
[c] Geologic Party No. 208, CNNC, 014000 Baotou, Inner Mongolia, China

ARTICLE INFO

Keywords:
Tamusu
Sandstone-type uranium deposit
Trace elements
Stable isotopes
Fluid inclusions
Hydrothermal fluids

ABSTRACT

The Tamusu deposit is a large sandstone-type uranium deposit discovered in recent years in the Bayingobi basin, Inner Mongolia. Hydrothermal activity was recorded by veins in this deposit, but its relationship with uranium mineralization has not been clarified. In this study, petrographic observations, chemical composition of U minerals, whole rock geochemistry, fluid inclusions and C–O–S stable isotope studies of sandstone and veins were integrated to characterize the mineralizing fluids and mineralization conditions. We found uranium minerals generally co-exist with pyrite occurring in interstitial pores or on detrital grains in sandstone. The main ore mineral is pitchblende, and minor ore minerals include brannerite and coffinite. Pitchblende coexists with subhedral pyrite, whereas brannerite and coffinite coexist with cubic pyrite and calcite. Calcite also occurs in veins together with gypsum. Fluid inclusions from calcite and gypsum in the veins have homogenization temperatures ranging from 124 °C to 326 °C, with salinities of 5.7–17.2 wt% NaCl equivalent. The C–O and S isotopes of the vein minerals suggest that the hydrothermal fluids were derived from circulated formation water. Trace element analysis shows that the U-bearing sandstone is commonly enriched in V, Re and Mo, while the high-grade uranium ores are further enriched in Zn, Co, Ni and Cu. The REE patterns and δEu values in the high-grade U-bearing sandstone are similar to those in the veins, which are characterized by high LREE and low δEu, suggesting that the high-grade U-bearing sandstone is related to hydrothermal activity. The mineral assemblages, temperatures, trace elements and isotopes indicate that the Tamusu deposit was affected by two distinct types of fluids: supergene diagenetic alkaline oxidizing fluids and acidic reducing hydrothermal fluids. The oxidizing fluids started to be involved after the deposition of the ore-hosting upper Bayingobi Formation, forming a large amount of low-grade U-bearing ores. The hydrothermal fluids occurred in association with the eruption of basalt in the overlying Suhongtu Formation. The involvement of hydrothermal fluids changed the pH and Eh conditions, superimposed and reformed the low-grade uranium ores, forming high-grade uranium ores, and finally fixed the position of the uranium orebodies. Therefore, the Tamusu deposit experienced four main stages: (i) sedimentary and early diagenetic uranium concentration, (ii) oxidation and ore-forming stage, (iii) hydrothermal alteration and superimposed mineralization, and (iv) post-ore stage.

1. Introduction

The genesis of sandstone-hosted uranium deposits is generally considered to be related to the interaction of oxidizing uranyl-bearing fluids with reducing agents within permeable sandstones, where soluble U (VI) is reduced to insoluble U (IV) by detrital plant debris, humates, hydrocarbons and sulfides (Curiale et al., 1983; Hansley and Spirakis, 1992; Spirakis, 1996). However, there are studies showing that some sandstone-type uranium deposits may also be closely related to deep fluid circulations in sedimentary basins (Ingham et al., 2014; Zhang et al., 2017). Close spatial association of uranium deposits and deeply sourced oil and gas deposits as well as intermediate-basic dikes has been identified in some sandstone-type uranium deposits in the East Asian Energy Metallogenic Mega Province (Liu et al., 2007; Lin et al.,

* Corresponding author.
E-mail address: 850359679@qq.com (C. Zhang).

https://doi.org/10.1016/j.oregeorev.2019.102999
Received 4 May 2018; Received in revised form 20 June 2019; Accepted 2 July 2019
Available online 03 July 2019
0169-1368/

2017), such as sedimentary basins in Kazakhstan and north China (Li et al., 2011; Aubakirov, 2016; Nie et al., 2017). Uranium deposits that have been modified by deep hydrothermal fluids are different from the typical interlayer oxidation deposits in morphology of orebodies, uranium minerals and alteration mineral assemblages (Adams, 1991; Fan et al., 2007; Nie et al., 2017). However, the role of hydrothermal activity in the mineralization of sandstone-type uranium deposits is still unclear, and most genetic models for sandstone-type U deposits do not consider the role of hydrothermal fluids (Zhang, 2016; Wang et al., 2017).

The Tamusu deposit, which was discovered in the Bayingobi basin in recent years, is a large sandstone-type uranium deposit. The development of numerous hydrothermal veins in the mineralization area suggests that the uranium mineralization may be related to hydrothermal fluids (Pan et al., 2009; Ding and Hou, 2012; Zhang et al., 2015). However, many previous studies suggest that the main orebodies are mainly controlled by the interlayer oxidation zone and the effect of hydrothermal activity should not be exaggerated (Wu et al., 2008; He et al., 2010; Shen et al., 2014). The uncertainty about the role of hydrothermal fluids for uranium mineralization is partly due to the lack of detailed geochemical study. Therefore, this study will focus on the characteristics of different fluids and their relationships with uranium mineralization.

Because of the sensitivity to environmental change, trace elements have become an increasingly important tool for determining the genetic conditions of U deposits (Deng et al., 2003; Bonhoure et al., 2007; Mercadier et al., 2011; Frimmel et al., 2014). The REEs are widely used to evaluate the role of hydrothermal fluids in U mineralization processes (Zhu et al., 2005; Mercadier et al., 2011; Frimmel et al., 2014; Zhang, et al., 2017). In this study, we analyzed the geochemical composition of the host sandstone and veins, including trace elements and REE concentrations of whole rocks, and the stable isotopes of S, C and O of separated minerals. Combined with petrography, we use the data of fluid inclusions, alteration minerals and uranium minerals to determine the physicochemical conditions, and evaluate whether hydrothermal fluids played an important role in uranium mineralization.

2. Geological setting

2.1. The Bayingobi basin

The Bayingobi basin is located in Inner Mongolia, and covers an area of 250,000 km^2. It is a pull-apart basin lying on a long-term active belt among the Kazakhstan, Siberia, Tarim and Sino Korean plates (Fig. 1). The basement of the basin is composed mainly of Paleozoic and early Mesozoic intermediate to felsic granitic plutons, mafic to felsic volcanic rocks, and Proterozoic to Paleozoic sedimentary or metasedimentary units (Meng et al., 2002). Parts of the granitic plutons mentioned above may be a primary uranium source for the basin-hosted uranium mineralization as some granites show high uranium content (4–13 ppm U) compared with the average in granites (U mean = 4 ppm, Cuney and Kyser, 2008). The Triassic and Jurassic strata are distributed only in the northwest area of the basin and consist of fluvial and lacustrine sandstone, shale, mudstone and coal seams. Cretaceous strata are the main sedimentary cover of all the depressions, which comprise alluvial fan and lacustrine facies (composed of conglomerates, sandstone, shale and sandy limestone). The Cretaceous strata can be divided into the Bayingobi Formation (K_1b), Suhongtu Formation (K_1s), Yingen Formation (K_1y) and Wulansuhai Formation (K_2w). The Cenozoic strata occur sporadically, comprising alluvial and fluvial deposits.

2.2. Uranium deposit geology

The Tamusu deposit was discovered in 2001 in the northern part of the Yingejin depression. The deposit is located to the southwest of Tamusu town, approximately 15 km northwest of Mount Zongnai, where the strata displays a southeast-dipping monocline. There are three NE trending concealed faults in the ore field, as revealed by a shallow seismic survey (Fig. 2).

The deposit is hosted within the early Cretaceous Bayingobi Formation and is positioned at depths between 180 and 610 m below the surface (Fig. 3). The Cretaceous and older strata crop out to the northwest of the deposit. The Bayingobi Formation unconformably overlies the Jurassic strata and unconformably underlies the late Cretaceous Wulansuhai Formation. The Wulansuhai Formation has been entirely eroded in some areas, where the Bayingobi Formation is exposed on the surface (Fig. 2).

The Bayingobi Formation is divided into an upper member and a lower member. The lower member is composed of purple to red conglomerate deposited in an alluvial fan system. The upper member is composed mainly of grey conglomerate and sandstone with abundant carbonaceous debris, carbonaceous silty mudstone, and dolomitic limestone, and was deposited in a semi-humid fan delta and lacustrine environment. The sandstone and mudstone in the Tamusu deposit are well consolidated, and have a large number of small vertical veins (Fig. 4A, B, C and D), which is in contrast to other sandstone-type uranium deposits. The high content of carbonate (average 8%) and gypsum (average 9%) in the sandstone matrix is the main reason for the general consolidation of the ore-hosting sandstone (Fig. 4B). Clay minerals are not well developed in the sandstone because of the strong cementation of carbonate and gypsum. On the west side of the deposit there is a high content of clay minerals in the green-grey sandstone, with chlorite being the main clay mineral.

3. Mineralization and alteration

3.1. Uranium mineralization

The orebodies are mostly tabular or lenticular in shape, and located at the top or bottom of the sand bodies (Fig. 3). Uranium mineralization is mainly hosted in organic matter- and pyrite-rich gray sandstone and silty mudstone (Fig. 4E and F). Thin-section observations and Electron Microprobe Analyzer (EMPA) analysis show that the U minerals include pitchblende, coffinite and brannerite. The uranium minerals generally coexist with pyrite occurring in interstitial pores or on the surface of detrital grains in the sandstone. The pyrite associated with the uranium minerals can be divided into four types: fine framboidal pyrite, subhedral pyrite crystals or aggregates, cubic pyrite and veinlet pyrite (Fig. 5A, B, C and D). Subhedral pyrite commonly coexist with pitchblende and a small amount of coffinite. In some cases, coffinite and brannerite are closely associated with calcite and galena (Fig. 5E and F). However, uranium minerals are rarely found in or around the hydrothermal veins.

3.2. Mineral paragenesis

Thin-section observations (Fig. 6) reveal that the minerals related to alteration and mineralization formed in four distinct stages as described below and summarized in Fig. 7.

3.2.1. Synsedimentary/early diagenetic uranium concentration stage

The upper member of the Bayingobi Formation sandstone in the Tamusu deposit is an immature, moderately to poorly sorted, angular to sub-angular lithic arenite, in which the detrital grains consist of quartz (16% to 31.8%), feldspar (10.7% to 26.7%) and rock fragments (20.8% to 45.5%). The rock fragments are composed of granite and quartzite. Framboidal pyrite, fine-grained pyrite and microcrystalline calcite are widely distributed (Figs. 5 and 6).

3.2.2. Oxidation and ore-forming stage

The mineral assemblages in this stage include limonite, hematite and some kaolinite, which occur mainly in the contact between the

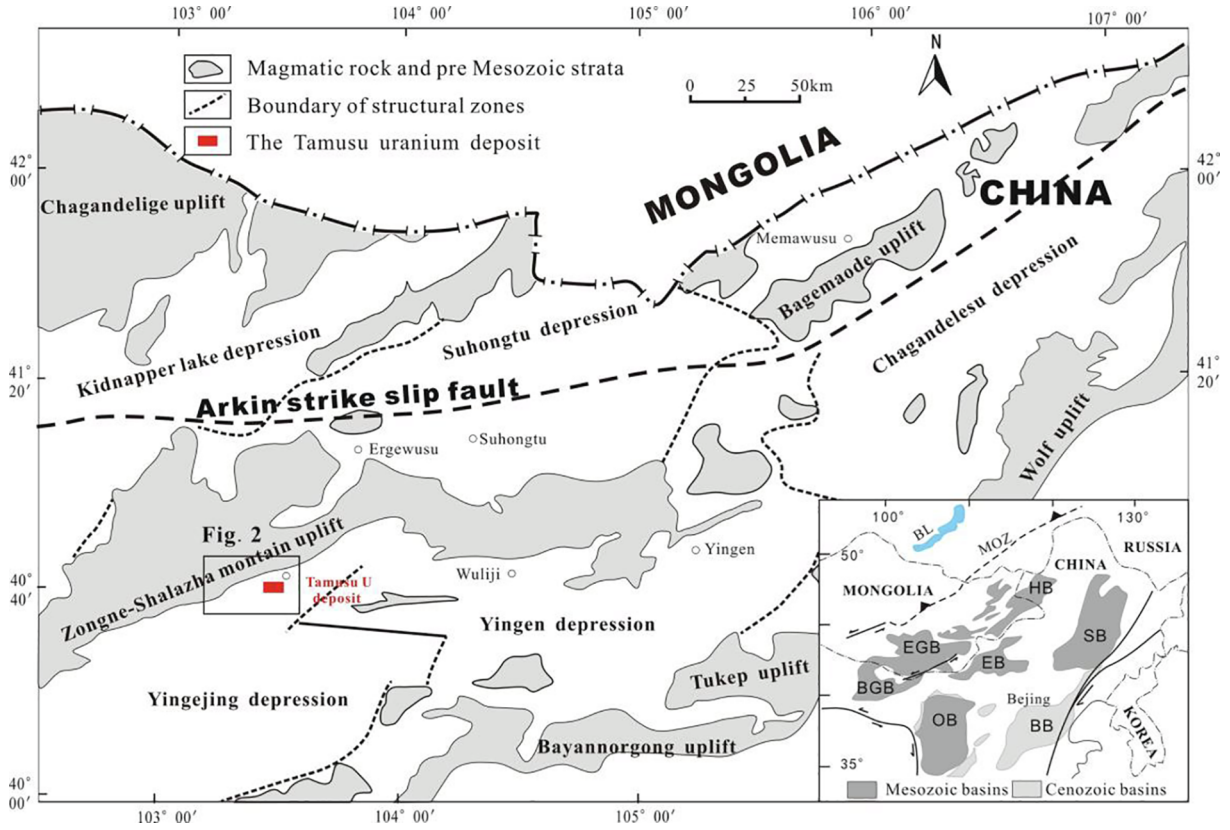

Fig. 1. Structural map of the Bayingobi Basin showing the distribution of uranium deposits and oil-bearing depressions (modified after Wei et al., 2006; Bonnetti et al., 2015; Meng et al., 2002). BB = Bohai Basin, EB = Erlian Basin, EGB = East Gobi Basin, HB = Hailar Basin, OB = Ordos Basin, SB = Songliao Basin, BGB = Bayingobi Basin, BL = Baikal Lake, MOZ = Mongol-Okhotsk Zone.

oxidized sandstone and gray sandstone. In the red or yellow sandstone, pyrite is oxidized to limonite (Fig. 6B), which is mostly in the form of patches or veins along the edge of the detrital grains. The uranium minerals occur mainly as pitchblende (5–9 μm), and small amounts of coffinite co-existing with subhedral pyrite (Fig. 5B and C). This is the main mineralization stage and the U minerals are mostly located in the oxidation-reduction transition interface, which is related to the early interlayer oxidation.

3.2.3. Hydrothermal alteration and superimposed mineralization stage

The red sandstone and gray sandstone in the Tamusu deposit are cut by many veins, indicating that hydrothermal fluids were involved after the interlayer oxidation stage. The minerals in the veins are composed mainly of pyrite, calcite, fluorite and gypsum and a small amount of bornite and sphalerite (Fig. 6G, H and I). Corroded coarse-grained calcite is encrusted in gypsum in the veins, suggesting that gypsum was formed after calcite (Fig. 6E).

Because of the hydrothermal activity, the ore-hosting sandstone has undergone significant alteration, mainly manifested by recrystallization and formation of new minerals. The recrystallization of argillaceous carbonate and framboidal pyrite is widespread, resulting in the formation of euhedral and subhedral coarse-grained carbonate minerals and cubic pyrite aggregates (Fig. 6C and F). A large number of dolomite and ankerite fine crystals are distributed along the edge or in the pores between detrital grains (Fig. 6D). The gypsum is always found enwrapping granular carbonate minerals and other minerals in the form of cementation (Fig. 6E), indicating that the gypsum was formed after these minerals.

The main uranium mineral assemblages at this stage are brannerite and coffinite co-existing with cubic pyrite, calcite and veinlet pyrite (Fig. 5D and E). Metallic sulfides are commonly found around the uranium minerals (Fig. 5F).

3.2.4. Post-ore stage

In this stage the hydrothermal event caused a general consolidation of the sandstone, terminated the migration of the oxidizing fluids in the sandstone pores, and finally fixed the position of the uranium orebodies. A large number of limonite and hematite veins are distributed in fissures (Fig. 4C), and a small amount of disseminated limonite is also found in the gypsum cementation, indicating that at this stage the oxidizing fluids mainly flowed along the fissures.

4. Sampling and methods

One hundred and twenty-five (125) samples were collected 32 drilled holes, and all of them were cut and made into thin sections for optical microscopy, scanning electron microscopy (SEM) and Electron Microprobe Analyzer (EMPA) observation. SEM equipped with an energy dispersive X-ray spectrometer (EDS) and EMPA analysis were conducted at Key Laboratory of Nuclear Resources and Environment, East China University of Technology, using Nova NanoSEM 450 SEM and JXA-8100M electron probe. The EMPA analytical conditions are as follows: acceleration voltage of 15 kV, current of 20nA, and beam spot diameter of < 2 μm, a 10 s counting time for the major elements, 20 s or 40 s for the minor elements.

The 20 samples for C–O isotope analysis were collected from three types of occurrences: grains of calcite from the veins, calcite cement in sandstone, and marl. It is noteworthy that the data of the first two types are from single minerals and last one represents whole-rock analysis. The 20 samples for S isotope analysis come from pyrite and gypsum in veins, fine grained pyrite in the sandstone, cubic pyrite in the sandstone, and gypsum cement in the sandstone.

Details of pre-analysis process for C–O–S isotope analyses are as follows: (1) For those minerals in the veins, the wall rock surrounding the veins were removed, and then the vein mineral grains (calcite,

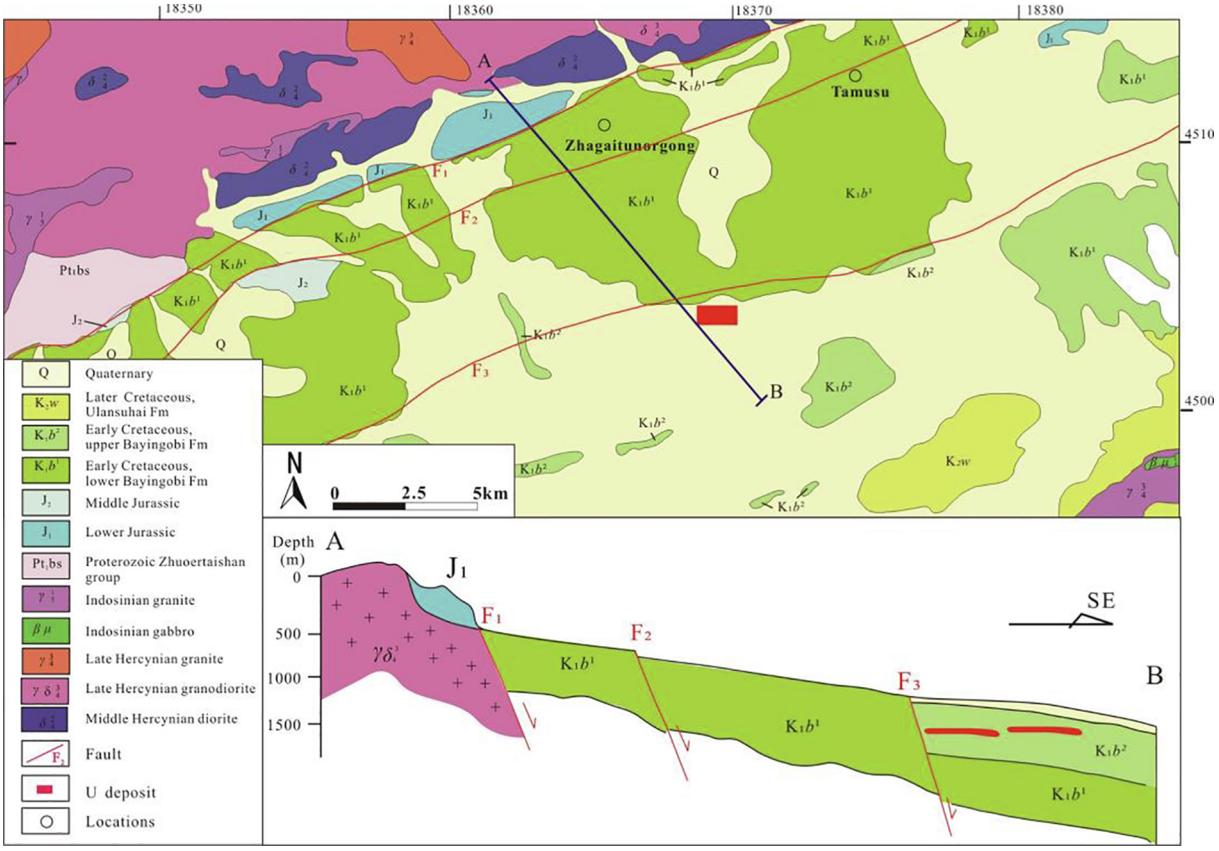

Fig. 2. A) Geological map of the northern part of the Yingejing Sag, Bayingobi Basin (modified after Zhang et al., 2015). This map shows the location of A-B cross-section presented in Fig. 2B. B) Cross-section of the Yingejin depression.

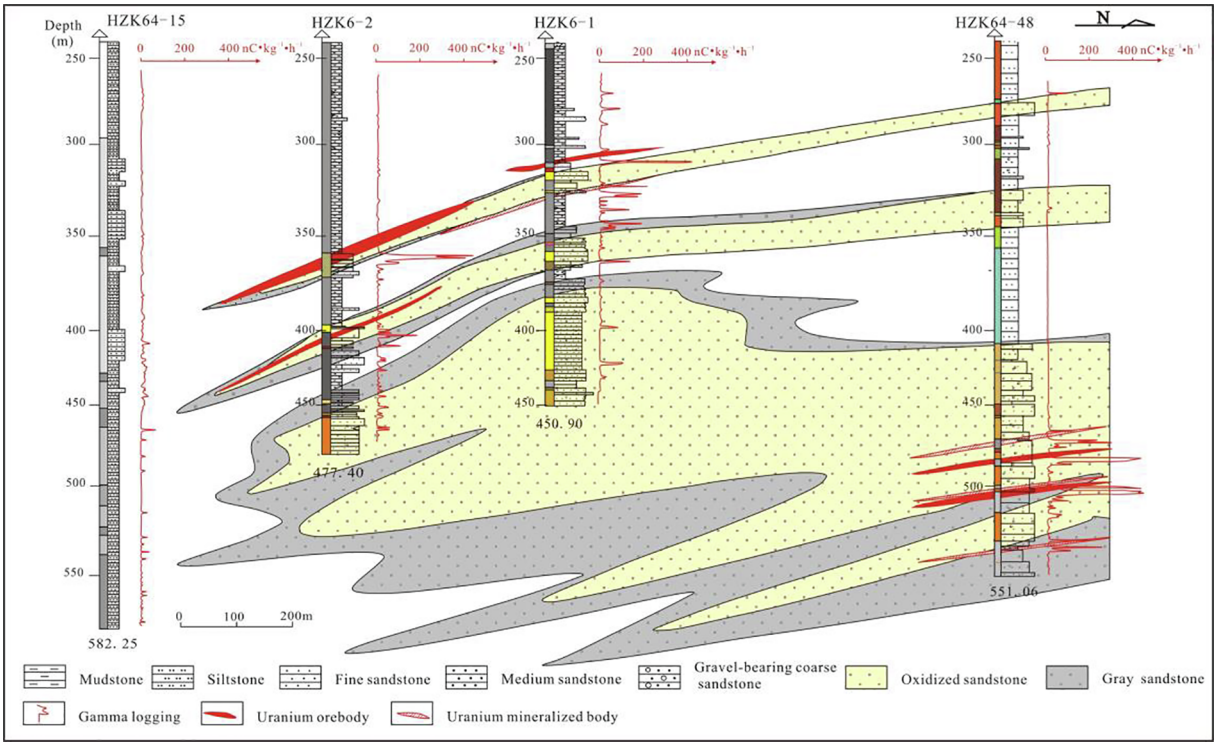

Fig. 3. Cross section showing tabular shape orebodies in the Tamusu deposit.

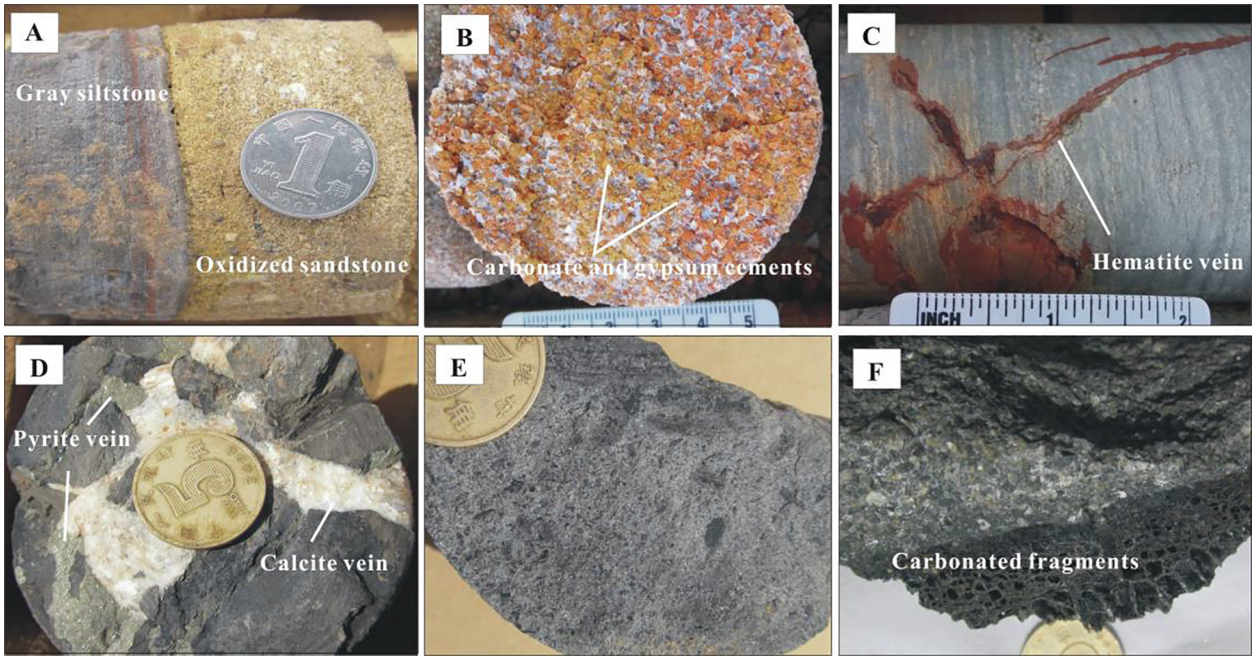

Fig. 4. Drill cores from the Tamusu deposit. A) Gray mudstone and oxidized sandstone; B) Gypsum cementation in oxidized sandstone; C) Distribution of hematite along fissures; D) Calcite and pyrite veins in mudstone; E) Siltstone U ore with carbonaceous debris; F) Sandstone U ore with carbonaceous debris.

pyrite, and gypsum, generally 1–20 g for each sample) were manually separated under the binoculars using tweezers; (2) For those minerals in the sandstone, including calcite cement, fine grained pyrite, cubic pyrite and gypsum cement, the rock samples were crushed firstly and then elutriated in water, and the individual minerals were hand-picked under the binoculars; (3) For thin marl layers (about 4–6 cm) intercalated in the sandstone, whole-rock samples were peeled out and then milled into powder. All minerals separated from veins or sandstones were washed in distilled water, dried naturally, and subsequently powdered for analysis.

Carbon and oxygen isotope analyses were carried out at the State Key Laboratory of Nuclear Resources and Environment, East China University of Technology, by using a MAT-253 mass spectrometer. Approximately 2–5 mg of powdered calcite sample reacted with anhydrous phosphoric acid at 25 °C to produce CO_2. The released CO_2 gas was introduced into the isotope ratio mass spectrometer and analyzed for the $^{13}C/^{12}C$ ratio. The analytical precision is typically better than 0.2‰. Carbon and oxygen isotope compositions are reported relative to the international PDB (Pee Dee Belemnite) standards. The empirical relationship ($\delta^{18}O_{SMOW} = 1.03086*\delta^{18}O_{PDB} + 30.86$) given by

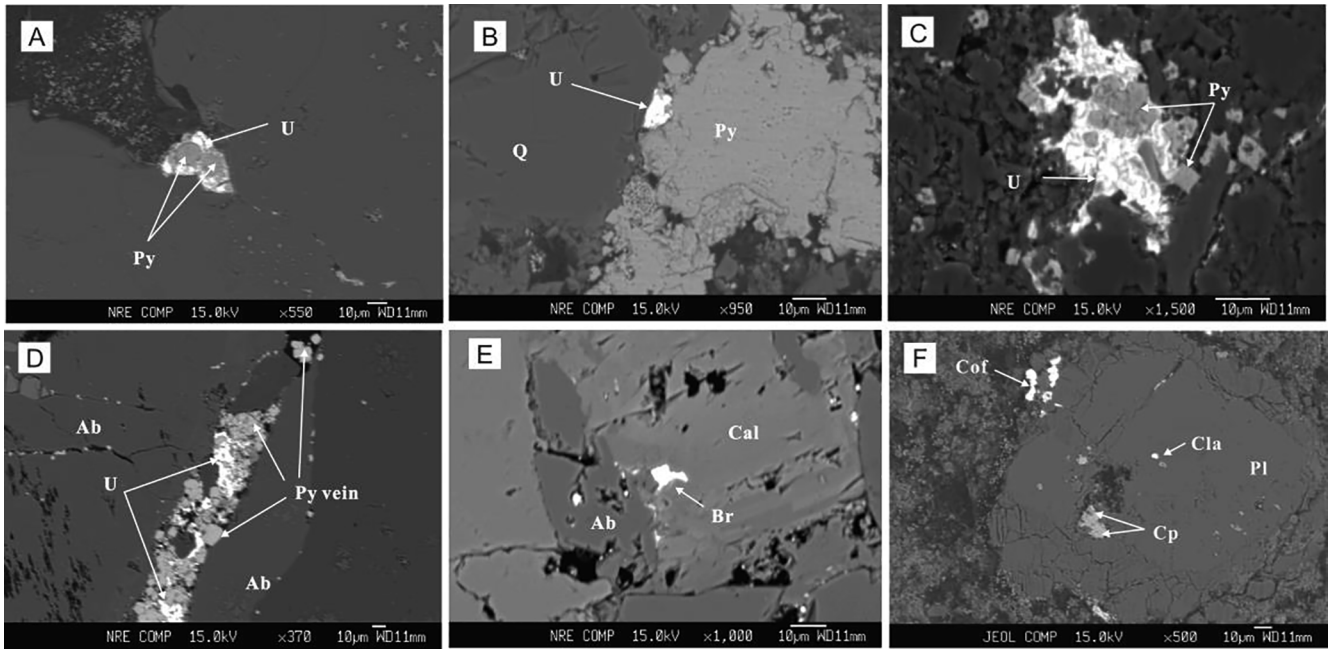

Fig. 5. Back-scattered electron images displaying the uranium mineralization and associated minerals from the Tamusu deposit. A) Pitchblende co-existing with framboidal pyrite; B) Pitchblende co-existing with pyrite aggregates; C) Pitchblende co-existing with subhedral pyrite; D) Brannerite co-existing with veinlet pyrite; E) Brannerite co-existing with coarse calcite cement with partial dissolution; F) Coffinite associated with chalcopyrite and clausthalite. Q = quartz; Py = pyrite; U = pitchblende; Cof = coffinite; Br = brannerite; Cal = calcite; Ab = Albite; Cla = clausthalite; Cp = chalcopyrite; Pl = plagioclase.

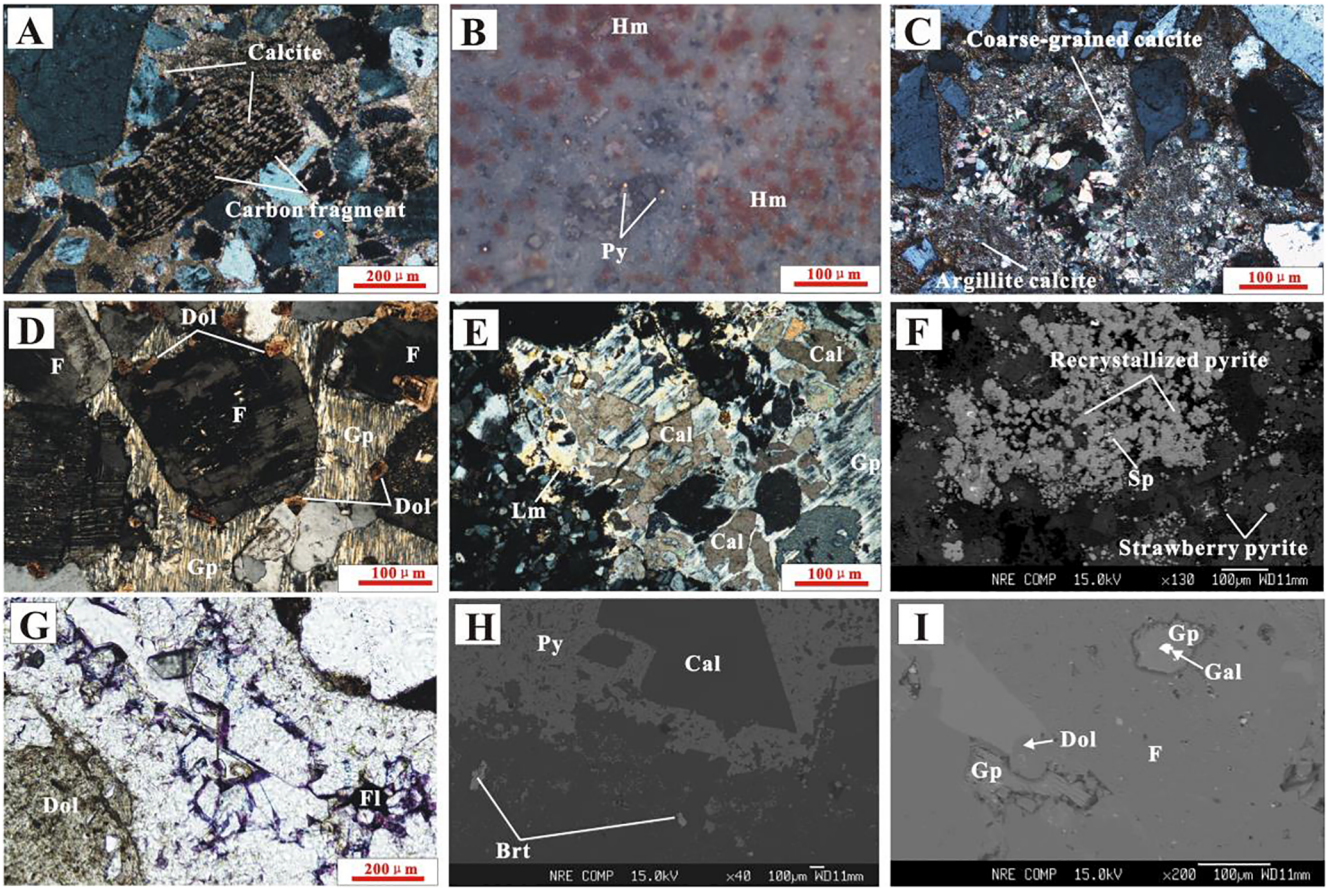

Fig. 6. Photomicrographs showing diagenetic minerals in the sandstone. A) Calcite associated with carbon fragment; B) Pyrite oxidized to hematite; C) Recrystallization of fine-grained calcite to coarse crystalline calcite; D) Euhedral dolomite cement and gypsum cement in sandstone; E) Gypsum encrusting and corroding coarse-grained calcite in veins with limonite on the edge of gypsum; F) Recrystallized subhedral pyrite associated with sphalerite; G) Fluorite vein in the dolomite cemented siltstone; H) Barite on the edge of pyrite and calcite vein; I) Galena in gypsum cement. Py = pyrite; Cal = calcite; Cla = clausthalite; Bar = barite; Gp = gypsum; Q = quartz; F = feldspar; Fl = fluorite; Gal = galena; S = sphalerite; Lim = limonite; He = hematite; Dol = dolomite; Bor = bornite.

Friedman and O'Neil (1977) was used for the conversion of the PDB standard to the SMOW standard. Carbon isotope fractionation is insensitive to temperature, and its value mainly reflects the mixing degree of different carbon sources, while oxygen isotope fractionation is significantly controlled by temperature (Huang et al., 2009; Conliffe et al., 2012). The oxygen isotope values of the hydrothermal fluids in equilibrium with calcite were calculated according to the empirical formula proposed by Zheng (1999) using the homogenization temperatures of fluid inclusions.

The sulfur isotope analyses were performed in the State Key Laboratory of Nuclear Resources and Environment, East China University of Technology. Samples were combusted at 1030℃ with O_2 and then analyzed using an elemental analyzer (Costech) coupled with a mass spectrometer (MAT-253). Standardization is based on international standards OGS-1 and NBS123 and several other sulfide materials that have been compared between laboratories. The precision is estimated to be ± 0.2‰ or better.

A total of 21 samples from different types of sandstone and calcite selected from veins were analyzed for trace element contents (Table 1). The samples were powdered in an agate mill to be 200 mesh for whole-rock analysis. Trace elements were measured by ICP-MS (NexION300D) at the Analytical Laboratory of Beijing Research Institute of Uranium Geology. Analyses of China Geological Survey standards GB/T 14506.30-2010 indicate that the precision and accuracy were better than 5% for the trace elements and REEs. The analysis was carried out at a temperature of 20℃ and a relative humidity of 27%. The REE contents were normalized to chondrite values (Sun and McDonough, 1989). Some parameters such as ΣREE, LREE/HREE, and δEu anomalies were calculated using the equations of Taylor and Mclennan (1985).

The samples used for fluid inclusion microthermometry were collected from gypsum and calcite veins. Microthermometric measurements were conducted at the Fluid Inclusion Laboratory of the State Key Laboratory of Nuclear Resources and Environment, East China Institute of Technology, using the Linkam THMSG600 heating-freezing stage. This instrument has a working temperature range from −196 °C to +600 °C and an accuracy of approximately ± 2 °C for homogenization temperatures and approximately ± 0.1 °C for the last ice-melting temperatures. The heating/freezing rate was 15 °C/min and reduced to 0.2 °C/min near the phase transformation points. Fluid salinities were estimated using final ice-melting temperatures for the NaCl-H_2O binary system (Bodnar, 1993).

5. Results

5.1. Trace elements and REE of whole rocks

The trace elements data for the whole-rock samples are shown in Table 2. Based on the color and uranium content, the sandstone samples were classified into the following categories: U-bearing sandstone (U = 100–1000 ppm), high grade U-bearing sandstone (U > 1000 ppm) and U-poor sandstone (U < 100 ppm).

The trace elements in the red or yellow U-poor sandstone and gray U-poor sandstone show similar patterns. The diagrams of trace elements of the veins are consistent with that of the U-poor mudstone samples, which

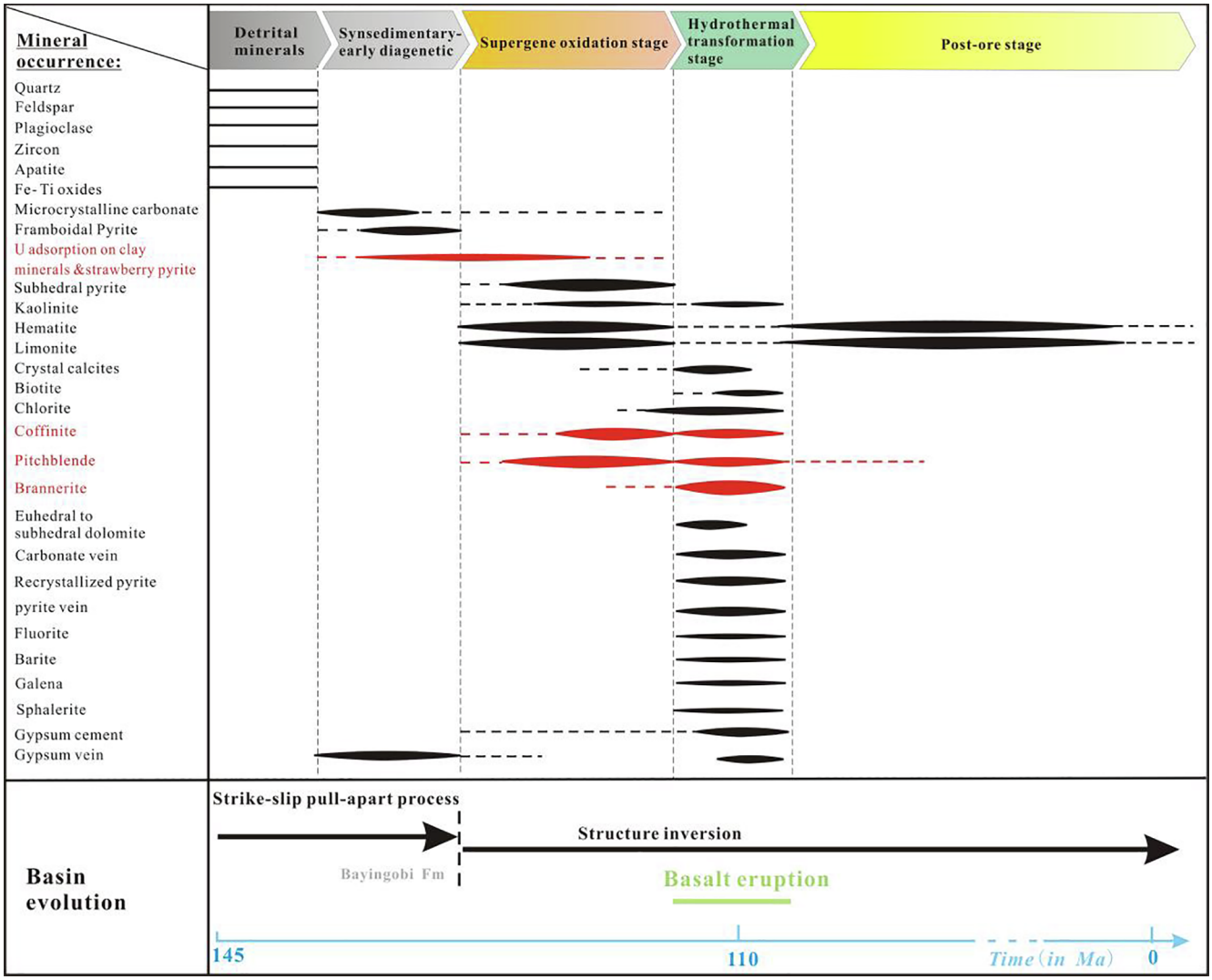

Fig. 7. Paragenetic sequences and tectonic events showing the different stages related to uranium mineralization of the Tamusu deposit.

Table 1
Detailed list of samples for trace elements in the Tamusu deposit.

Sample	Types	Location	Lithology	Attitude
B19	red or yellow U-poor sandstone	ZKH40-16, 648 m	red coarse-grained sandstone	oxidation zone above orebody
T10		ZKH96-16, 468.6 m	purple-red medium-grained sandstone	oxidation zone above orebody
T18		ZKH80-7, 478.9 m	purple-red fine sandstone	oxidation zone above orebody
B11		ZKH64-52, 486.5 m	red coarse-grained sandstone	oxidation zone above orebody
T63		ZKH112-16, 525.3 m	yellow medium sandstone	oxidation zone above orebody
B05	high grade U-bearing sandstone	ZKH60-52, 514.8 m	gray coarse-grained sandstone	ore
BN11		ZKH32-0, 529.7 m	dark gray fine-grained sandstone	ore
B12		ZKH56-44, 518.3 m	gray medium-grained sandstone	ore
T30	U-bearing sandstone	ZKH80-0, 430 m	argillaceous medium-grained sandstone with pyrite crystal	ore
B25		ZKH64-36, 558.5 m	gray coarse-grained sandstone	ore
B28	gray U-poor sandstone	ZKH60-16, 547.2 m	gray coarse-grained sandstone	reduction zone under orebody
B44		ZKH60-44, 508 m	gray coarse-grained sandstone	reduction zone between orebodies
B24		ZKH64-52, 552 m	gray fine-grained sandstone	reduction zone between orebodies
B55		ZKH60-40, 536.9 m	gypsum cemented gray conglomerate	reduction zone between orebodies
T92		ZKH88-64, 329.4 m	dark gray coarse sandstone with pyrite and carbon detrital grains	reduction zone above orebody
T23	U-poor mudstone	ZKH160-80, 527 m	dark-gray mudstone	between orebodies
T24		ZKH60-16, 521 m	dark-gray mudstone	between orebodies
T48		ZKH96-63,518 m	gray mudstone	above orebody
T26	veins	ZKH112-16, 512 m	gypsum vein in fine sandstone	cutting through the layer
T90		ZKH88-64, 416 m	gypsum vein in gray gravelly coarse-grained sandstone	cutting through the layer
B54		ZKH64-40, 528 m	pyrite vein in gray siltstone	cutting through the layer

Table 2
Representative trace elements concentrations for different types of samples in the Tamusu deposit (in ppm).

Sample	Red or yellow U-poor sandstone					High grade U-bearing sandstone			U-bearing sandstone		Gray U-poor sandstone					U-poor mudstone			veins		
	B19	T10	T18	B11	T63	B05	BN11	B12	T30	B25	B28	B44	B24	B55	T92	T23	T24	T48	T26	T90	B54
Sc	10.6	5.32	6.27	2.98	3.6	12.4	8.09	9.89	4.81	12	3.01	4.77	1.41	8.41	3.61	17.6	15.2	17.4	17.6	8.9	7.2
V	23.4	12.9	28.8	39.9	15.1	116	51.5	78.3	24.7	83.7	19.1	45.3	13.1	35.8	23.6	79.7	91.2	137	94.5	27.7	95.9
Cr	7.22	9.31	7.17	112	11.6	99.1	18.9	97.2	20.5	115	99.4	122	137	10.5	7.64	49.3	50.1	56.3	49.9	25.2	58.1
Co	4.02	3.41	3.12	2.71	3.33	33.4	16.3	13.8	12.7	4.19	2.41	2.28	3.1	5.33	2.07	14.8	15.9	14.2	14.2	7.52	18.9
Ni	6.74	5.61	9.58	4.36	6.02	47.1	34.8	19.5	27.7	10.6	5.78	5.14	5.58	11.7	7.52	24.2	25.5	25.8	30	13.5	32.3
Cu	15.1	6.51	4.97	3.39	9.03	10	14.5	22.3	16.5	8.59	2.88	2.77	7.59	10.1	4.79	25.4	21.9	34.5	29.9	16	44.8
Zn	9.28	14.1	25.3	15.3	21.6	195	208	190	18.2	9.19	11.5	18.1	26.2	16.1	6.4	91.2	113	89.7	111	110	130
Rb	66.4	67.3	54.8	74.5	73.4	71.5	39.4	119	61.3	84.4	53.4	73.8	71.2	90	67.4	126	129	109	124	76.7	155
Y	10.5	4.04	4.58	7.38	2.59	21.4	13.4	16.9	3.84	12.6	8.78	7.33	4.79	4.08	5.59	26.6	33.9	19.3	20.2	6.74	11.2
Nb	2.49	3.4	1.43	2.29	6.23	5.52	3.57	4.73	3.04	1.21	1.1	0.886	7.88	1.36	1.04	12.7	11.1	10.4	12.4	10.5	11.1
Mo	0.76	6.69	6.13	1.43	7.53	8.75	320	50.8	67.2	2.85	1.66	3.54	3.49	5.29	9.01	1.9	0.784	2.83	1.14	13.1	2.28
Cd	0.032	0.06	0.045	0.068	0.029	2.5	2.59	0.86	0.231	0.034	0.029	0.031	0.039	0.028	0.043	0.089	0.151	0.115	0.38	0.051	0.131
In	0.009	0.011	0.009	0.026	0.018	0.04	0.062	0.06	0.02	0.018	0.013	0.011	0.021	0.012	0.009	0.054	0.075	0.058	0.058	0.028	0.078
Ba	461	490	443	512	470	526	279	348	368	679	425	598	426	966	501	475	258	325	334	451	222
Ta	0.297	0.419	0.258	0.343	0.69	0.663	0.757	0.609	0.315	0.123	0.193	0.12	1.03	0.215	0.167	1.02	0.894	0.83	0.953	0.902	0.899
Re	0.004	0.002	0.019	0.005	0.006	3.39	3.08	3.58	0.528	0.006	0.01	0.001	0.001	0.001	0.024	0.02	0.008	0.001	0.006	0.011	0.001
Tl	0.783	1.06	1.76	3.94	1.98	10.9	7.72	3.87	9.81	3.67	2.01	1.86	0.997	0.868	3.62	0.773	0.779	0.82	0.827	0.65	7.13
Pb	13.3	14.7	15	18.9	12.9	41.8	28.7	29.6	20.3	18.3	12.7	14.1	15.1	15.1	14	18.9	18.7	15.2	21.4	18.5	22
Bi	0.105	0.063	0.064	0.389	0.099	1.98	0.224	0.338	0.123	0.29	0.239	0.117	0.229	0.069	0.06	0.647	0.665	0.527	0.629	0.241	0.753
Th	7.35	1.39	1.37	1.51	0.749	3.99	12	4.67	1.69	15.3	5.23	1.62	2.22	0.786	7.55	15.3	27.3	9.33	12.7	2.44	8.02
U	22.7	2.63	5.06	16.1	3.68	7000	5963	1363	167	135	5.28	4.13	4.56	2.51	2.22	15	12.7	5.74	7.53	6.28	3.24
La	9.03	9.98	8.65	20.3	4.18	34.6	40	38.4	8.07	16.6	11.7	13.6	16	7.5	11	41.4	48.6	28.7	29.3	18.3	36.2
Ce	16.6	18.7	15.4	38.2	6.48	56.7	83.8	68.5	12.1	35.2	22.2	23.4	27.5	13.4	19.6	75.7	101	53.1	55.4	32.3	68.2
Pr	1.95	2.2	1.67	4.55	0.708	6.31	10.1	7.96	1.2	3.62	2.53	2.51	2.89	1.56	2.25	8.64	11.3	6.36	6.48	3.51	7.54
Nd	8.35	8.47	5.82	16.2	2.53	23	39.9	30.6	4.15	13.9	9.85	8.93	9.89	6.23	8.24	32.9	44.1	24.7	25.1	12.1	28.2
Sm	1.56	1.41	0.914	2.23	0.448	4.03	6.09	6.17	0.67	2.43	1.88	1.42	1.36	0.88	1.4	5.84	8.15	4.59	4.64	2.03	4.41
Eu	0.541	0.442	0.309	0.58	0.244	0.94	1.36	1.35	0.292	0.683	0.521	0.463	0.4	0.437	0.434	1.22	1.53	1	0.942	0.534	0.906
Gd	1.75	1.1	0.829	1.82	0.408	3.58	5.32	5.18	0.672	2.19	1.67	1.24	1.2	1.93	1.37	5.2	7.22	4.02	4.08	1.75	3.64
Tb	0.268	0.174	0.143	0.31	0.075	0.677	0.767	0.901	0.117	0.402	0.316	0.236	0.199	0.133	0.225	0.937	1.25	0.692	0.703	0.295	0.527
Dy	1.5	0.799	0.802	1.42	0.42	3.82	3.59	4.08	0.634	2.18	1.71	1.34	0.933	0.829	1.05	4.88	6.43	3.5	3.49	1.33	2.47
Ho	0.352	0.148	0.158	0.251	0.087	0.736	0.431	0.66	0.128	0.444	0.306	0.261	0.167	0.118	0.194	0.953	1.25	0.667	0.677	0.24	0.445
Er	1.29	0.405	0.447	0.794	0.245	2.3	1.22	1.9	0.362	1.58	0.891	0.831	0.524	0.42	0.528	2.6	3.27	1.82	1.9	0.675	1.19
Tm	0.291	0.067	0.079	0.121	0.049	0.391	0.211	0.291	0.063	0.338	0.141	0.141	0.083	0.072	0.093	0.444	0.543	0.313	0.332	0.123	0.19
Yb	1.81	0.416	0.463	0.794	0.326	2.53	1.62	1.9	0.395	2.88	0.887	0.948	0.555	0.49	0.57	2.7	3.32	1.93	2.16	0.843	1.36
Lu	0.237	0.058	0.068	0.12	0.048	0.375	0.274	0.28	0.06	0.585	0.13	0.143	0.085	0.072	0.078	0.381	0.458	0.271	0.309	0.121	0.198
ΣREE	45.53	44.37	35.75	87.69	16.25	139.99	194.68	168.17	28.91	83.03	54.73	55.46	61.79	34.07	47.03	183.80	238.42	131.66	135.51	74.15	155.48
LREE	38.03	41.20	32.76	82.06	14.59	125.58	181.25	152.98	26.48	72.43	48.68	50.32	58.04	30.01	42.92	165.70	214.68	118.45	121.86	68.77	145.46
HREE	7.50	3.17	2.99	5.63	1.66	14.41	13.43	15.19	2.43	10.60	6.05	5.14	3.75	4.06	4.11	18.10	23.74	13.21	13.65	5.38	10.02
LREE/HREE	5.07	13.01	10.96	14.58	8.80	8.72	13.49	10.07	10.89	6.83	8.05	9.79	15.49	7.38	10.45	9.16	9.04	8.96	8.93	12.79	14.52
δEu	1.00	1.05	1.06	0.85	1.71	0.74	0.71	0.71	1.32	0.89	0.88	1.04	0.94	1.00	0.95	0.66	0.60	0.70	0.65	0.85	0.67

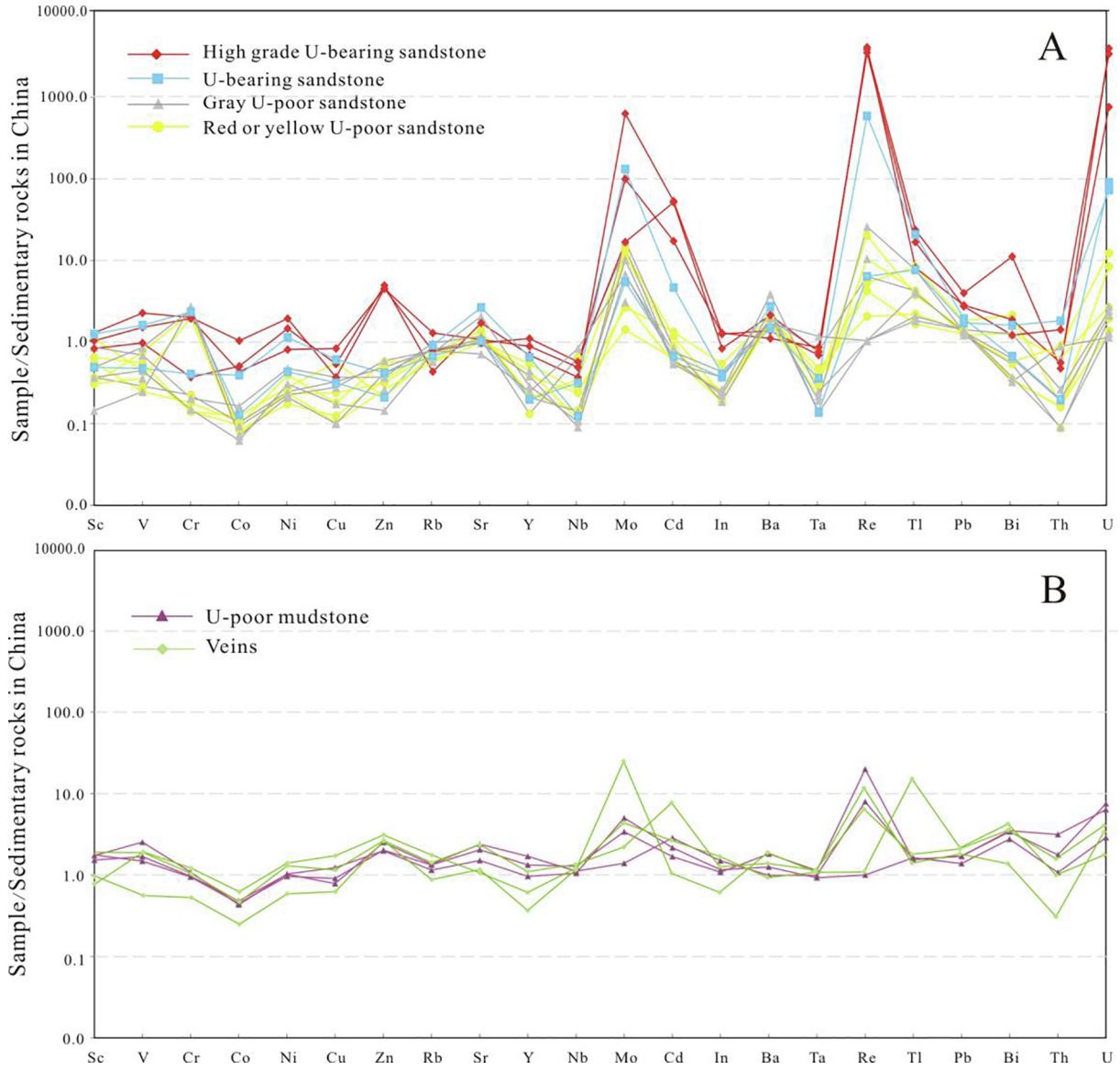

Fig. 8. Characteristics of trace elements in different samples normalized to average sedimentary rocks in China (Li, 1994). A) Samples of different types of sandstone, B) Samples of mudstone and vein.

differ from those of the sandstone samples (Fig. 8A and B). The Zn, Cd, U and Re contents in the samples of high-grade U-bearing sandstone (Zn = 190.0–208.0 ppm; Cd = 0.8–2.5 ppm; U = 1363.0–7000.0 ppm; Re = 3.1–3.6 ppm) are about 10 times higher than in the U-bearing sandstone. The concentrations of Co, Ni, Mo, Y, Cu and V in the high-grade U-bearing sandstone (Co = 13.8–33.4 ppm; Ni = 19.5–47.1 ppm; Mo = 8.7–320.0 ppm; Y = 13.4–21.4 ppm; Cu = 10.0–22.3 ppm; V = 51.6–116.0 ppm) are about 2–5 times higher than those in the U-bearing sandstone. The U-bearing sandstone samples are enriched in V, Re and Mo, and U is positively correlated with V, Mo and Re. The high-grade U-bearing sandstone samples are also enriched in Zn, Cu, Co and Ni, and U is positively correlated with Zn, Co and Ni (Fig. 9). The Co, Ni, Cu, Y, Bi and Zn contents in the high-grade U-bearing sandstone are much higher than that in the other types of sandstone, but consistent with that of the veins (Fig. 10).

The analytical results indicate that the total REEs of the U-bearing sandstone ranged from 28.91 to 83.03 ppm with an average of 55.97 ppm, which is consistent with that of the gray U-poor sandstone (34.07–61.79 ppm) and red or yellow U-poor sandstone (16.25–87.69 ppm). The high-grade U-bearing sandstone is significantly enriched in total REEs (Table 2), ranging from 139.99 to 194.68 ppm with an average of 167.61 ppm, which is similar to that of the U-poor mudstone (131.66–238.42 ppm) and veins (74.15–155.48 ppm). The REE patterns of the high-grade U-bearing sandstone are consistent with those in the veins, and distinctly different from the patterns of the other sandstones (Fig. 11A and B). The ratios of light to heavy REE (LREE/HREE) of all the samples have similar variation characteristics, showing relatively LREE-enriched patterns. The δEu values of the high-grade U-bearing sandstone (average = 0.72), U-poor mudstone (average = 0.65) and veins (average = 0.72) are lower than those of the red or yellow U-poor sandstone (average = 1.13), gray U-poor sandstone (average = 0.96) and U-bearing sandstone (average = 1.10).

5.2. Fluid inclusions

Two types of fluid inclusions were identified on the basis of petrography of the hydrothermal veins in the Tamusu deposit, namely primary fluid inclusions and secondary fluid inclusions. Primary fluid inclusions were found in the gypsum veins and some calcite veins, and the inclusions are normally 3–20 μm in size with an irregular rectangular

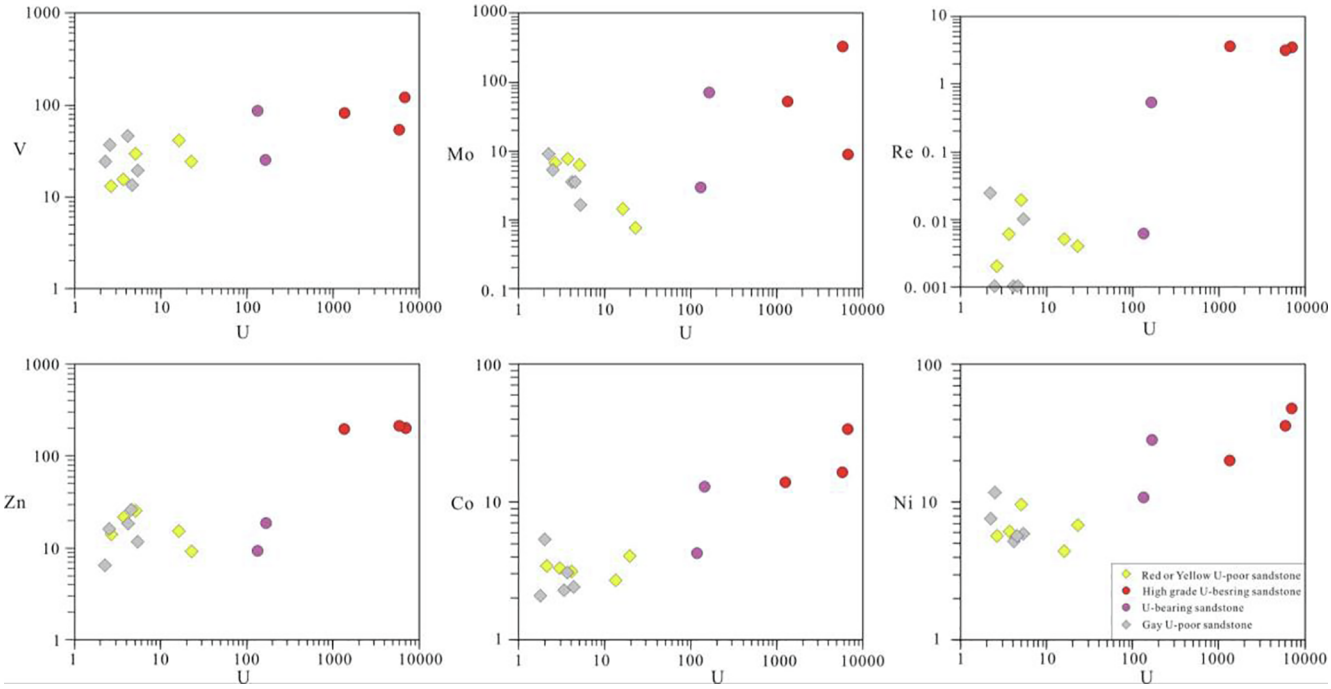

Fig. 9. Diagrams for selected elements showing correlations between V, Mo, Re, Zn, Co, Ni values vs. U contents for sandstone samples from the Tamusu deposit.

shape (Fig. 12). The fluid inclusions in gypsum are arranged in growth zones or randomly distributed, with similar liquid-vapor ratios and dominated by liquid phase. The fluid inclusion assemblages in the calcite veins appear generally in clusters or randomly distributed (Fig. 12). These fluid inclusions have similar gas/liquid ratios. Liquid-only inclusions are developed in both gypsum and calcite, and they are considered to be secondary in origin. Only primary inclusions were studied.

The homogenization temperatures (T_h), final ice-melting temperatures ($T_{m,\ ice}$), and salinities of the primary fluid inclusions from the Tamusu U deposit are given in Table 3. Homogenization temperatures (T_h) of fluid inclusions range from 205 °C to 278 °C, with the majority in the range from 220 °C to 280 °C (Fig. 13A). The final ice-melting temperatures ($T_{m,\ ice}$) vary from −17.3 °C to −5.4 °C, with corresponding salinity values ranging from 8.3 to 20.7 wt% NaCl equivalent (Fig. 13B), mainly in the range of 12–18 wt% NaCl equivalent.

5.3. Stable isotopic geochemistry

The $\delta^{34}S_{CDT}$ values of the microcrystalline and framboidal pyrite from the U-poor sandstone or mudstone range from −38.4‰ to −24.0‰, indicating biogenic origin. The $\delta^{34}S_{CDT}$ values of microcrystal pyrite in U-bearing sandstone range from −12.2 to −0.3‰. The $\delta^{34}S_{CDT}$ values of pyrite in veins have a wide range from −40.1 to −5.4‰, gradually decreasing with depth. The $\delta^{34}S_{CDT}$ values of gypsum are 11.3 to 11.9‰ in the sandstone and −30.0‰ to 10.0‰ in the vein (Table 4 and Fig. 14A).

The $\delta^{13}C_{PDB}$ values of the calcite cements in the red or yellow U-poor sandstone are relatively low, ranging from −4.6‰ to −1‰ and averaging −3.0‰, compared with the gray sandstone (−6.8 to +1.8‰, average +0.37‰). The $\delta^{13}C_{PDB}$ values of the mudstone samples are high, ranging from −1.6 to +3.5%, with an average of +2.8‰. The $\delta^{13}C_{PDB}$ values of the veins are similar to those in the sandstone, ranging from −4.5 to +0.5‰, with an average of −2.3‰. The $\delta^{18}O_{PDB}$ values of carbonate cement of the sandstone show a narrow range from −10.6‰ to −14.7‰, except two samples (−3.5‰ and −7.8‰). The $\delta^{18}O_{PDB}$ values of mudstone and vein have a wide range of variation, ranging from −3.2‰ to −12.1‰ and −7.7‰ to −17.1‰, respectively (Table 4 and Fig. 14B).

6. Discussion

6.1. Types and characteristics of fluids

Based on the above study results, there are two different types of fluids associated with the Tamusu deposit, which are different from typical sandstone-type uranium deposits including tabular or roll-front deposits (Cuney and Kyser, 2008; Harshman, 1972; Penney, 2012).

6.1.1. Supergene oxidizing fluids

The mineral associations of hematite and limonite indicate that the sandstone was affected by the action of oxidizing fluids. The $\delta^{13}C_{PDB}$ values of the carbonate cements in the oxidized sandstone show similar characteristics to those in meteoric water ($\delta^{13}C_{PDB}$ ranging from −5‰ to −1‰ according to Jansa and Noguera Urrea, 1990; Yang et al., 2009; Wei et al., 2015), indicating that the supergene oxidizing fluids are dominated by meteoric water, the pH of which depends on the surface environments. In general, calcium carbonate and other alkaline substances from dust can easily neutralize the acidic components (CO_2 and SO_2) of rainwater; hence, meteoric water is generally alkaline in arid climates (Worden and Morad, 2003). From the end of the early Cretaceous until now, the Bayingobi Basin has been in an arid climate (Wei et al., 2006). The pH values of the present surface-water and groundwater range from 8 to 9, indicating that the oxidizing water are alkaline fluids. Studies show that feldspar and other minerals are easily dissolved in an acidic solution but barely soluble under alkaline conditions (Fan et al., 2007; Li et al., 2011). Observation under microscope shows that clay minerals are rarely found in oxidized sandstone, which also confirms that the oxidizing fluids are alkaline.

6.1.2. Deeply sourced hydrothermal fluids

It is generally thought that the assemblage of fluorite, calcite and pyrite indicate a medium to low temperature acid-neutral environment (Zhao and Zheng, 1983; Guan et al., 2006), and that metallic sulfide minerals represent a strong reduction environment. Therefore, the hydrothermal fluids in the Tamusu deposit are considered to be reducing

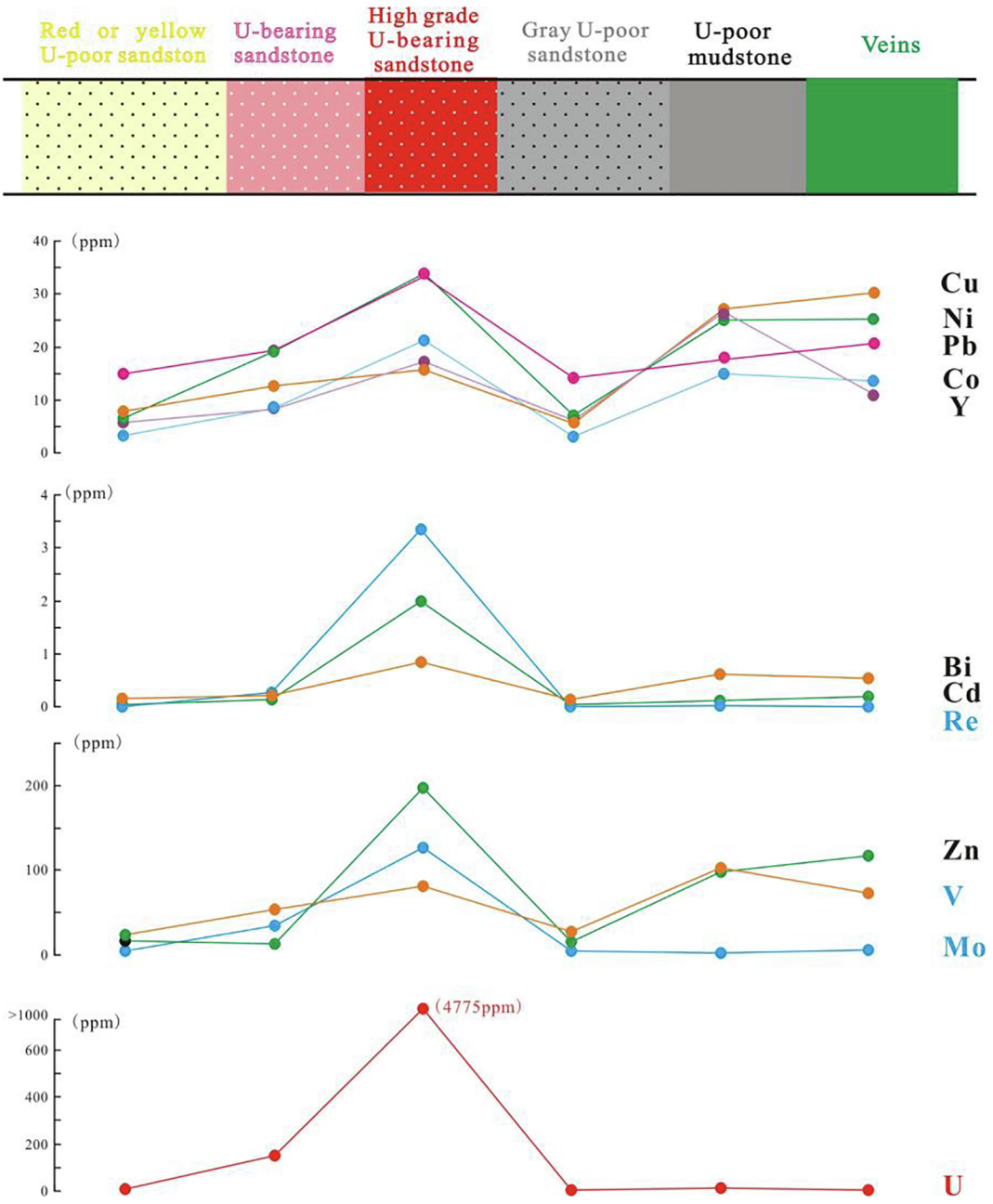

Fig. 10. Variation of trace elements in different zones related to U mineralization (Data represent average values).

acidic fluids.

In the early stage of hydrothermal events, recrystallization of coarse-grained carbonate and dolomite occurred with the increase of temperature, indicating that the diagenetic fluids in this period were mainly weak alkaline fluids (Wei et al., 2015; Zhang et al., 2017). Then, with the emergence of the deep acidic reducing hydrothermal fluids and organic acids from the organic matters in the sandstone (Zhu et al., 1996), the diagenetic environment became acidic, which is reflected by the significant dissolution of calcite and dolomite encapsulated in gypsum cement (Fig. 6E).

In the present-day mantle, the $\delta^{13}C_{PDB}$ value is considered to be about −5‰ (Taylor, 1986; Hoefs, 1987), while $\delta^{13}C_{PDB}$ related to organic matter is significantly lighter, generally between −4.0‰ and −35.0‰ (Suess and Whiticar, 1989; Ohmoto and Goldhaber, 1997). The $\delta^{13}C_{PDB}$ values of the carbonate cements and veins in the Tamusu deposit are mostly between −3.4‰ and +3.5‰, which is consistent with that of marine carbonate rocks (from −4.0‰ to +4.0‰, Claypool et al. 1980). The low $\delta^{13}C_{PDB}$ values in three vein samples suggest that the hydrothermal fluids may have been affected by organic matter. The $\delta^{18}O_{SMOW}$ values of the hydrothermal fluids in the Tamusu deposit (5.78‰ to 15.47‰) are different from that of magmatic water (5.5‰ to 9.5‰) as defined by Ohmoto (1986) and Sheppard (1986), and are compatible with basinal fluids that have experienced significant fluid-rock reaction.

It is generally recognized that sulfur isotopes with strongly enriched light isotopes (i.e., low $\delta^{34}S_{CDT}$ values) reflect the action of bacteria (Reynolds and Goldhaber, 1982; Hoefs, 1987; Min et al., 2005; Wu et al., 2015). The fact that $\delta^{34}S_{CDT}$ values of the pyrite in the veins decrease with increasing depth and the hydrothermal fluids have high salinities (> 12 wt% NaCl equivalent), suggests that the hydrothermal fluids may originate mainly from the formation water in the deep strata, as also reflected by the oxygen isotope data discussed above.

Previous studies have shown that the Yingejin sag has been in a state of uplifting since the late Early Cretaceous (Wei et al., 2006; Han,

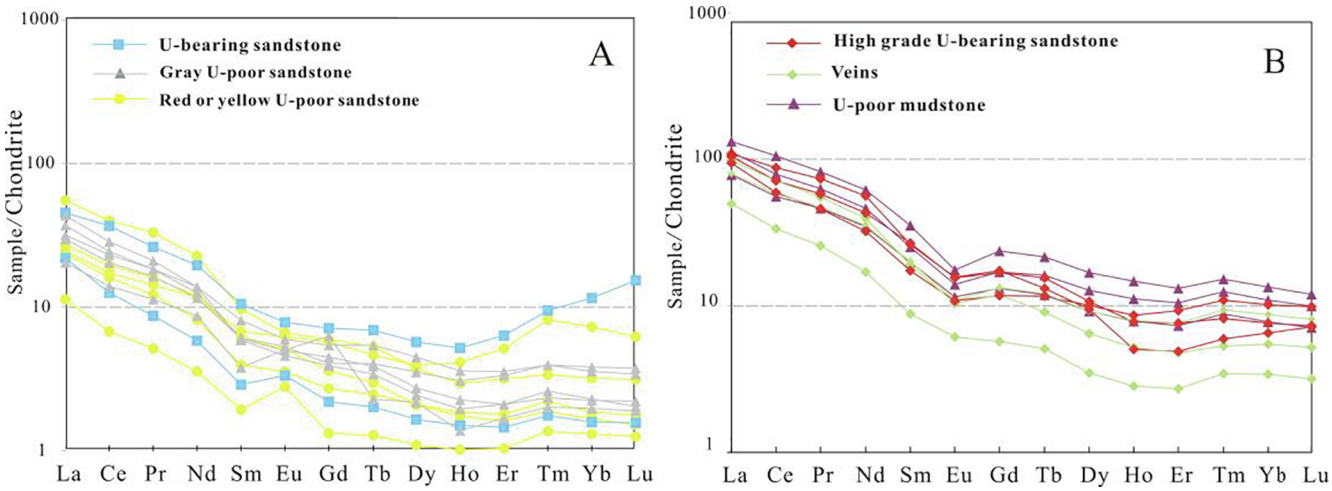

Fig. 11. REE patterns of different samples in the Tamusu deposit. A) Samples of different types of sandstone, B) Samples of high-grade sandstone, mudstone and vein.

2017), and the compaction of the sandstone is very weak (as reflected by the dominance of point contact of the clastic grains), therefore, the hydrothermal event could not have been caused by deep burial. Two volcanic events occurred in the basin after the deposition of the Bayingobi Formation: the late Early Cretaceous and the Late Cretaceous volcanic rocks. The late Early Cretaceous intermediate-basic volcanic rocks are widely distributed, with K-Ar ages ranging from 104.4 Ma to 116.7 Ma (Wei et al., 2006; Wu et al., 2010; Zhong et al., 2014), corresponding to the sedimentary period of the Suhongtu Formation. The Late Cretaceous volcanic rocks are mainly distributed in the margin of the basin, with K-Ar ages ranging from 65.6 Ma to 70.5 Ma (Wei et al., 2006). However, the two volcanic activities did not develop in the sag where the Tamusu deposit is located. The U-Pb isochron age of the uranium ores in the Tamusu deposit is 111.6 ± 8.1 Ma (Geological Team No. 208, CNNC, 2012, unpublished), which is consistent with the age of the volcanic rocks in the late Early Cretaceous, suggesting that the hydrothermal event is related to the formation of the high-grade uranium ores.

6.2. Relationships between hydrothermal fluids and uranium enrichment

Similar to U, the mobility of V, Mo and Re is also predominantly controlled by the redox condition (Abzalov, 2012; Granger and Warren, 1978; Harshman, 1972; Min et al., 2005). It has been noticed that the enrichment of U is closely related to these elements in sandstone-type uranium deposits in the Colorado Plateau, Yili basin in China, and many other basins (Wulser et al., 2011; Wang et al., 2005; Liam and John, 2017; Zhang et al., 2017). The Tamusu deposit also has similar characteristics: (i) The trace elements (V, Mo and Re) are controlled by redox conditions and are enriched in U-bearing sandstone and positively correlated with U. (ii) Uraninite is found generally associated with framboidal pyrite and organic matter. (iii) The orebodies are distributed on the top or bottom of the oxidation zones.

However, the distinctive characteristics of the trace elements and

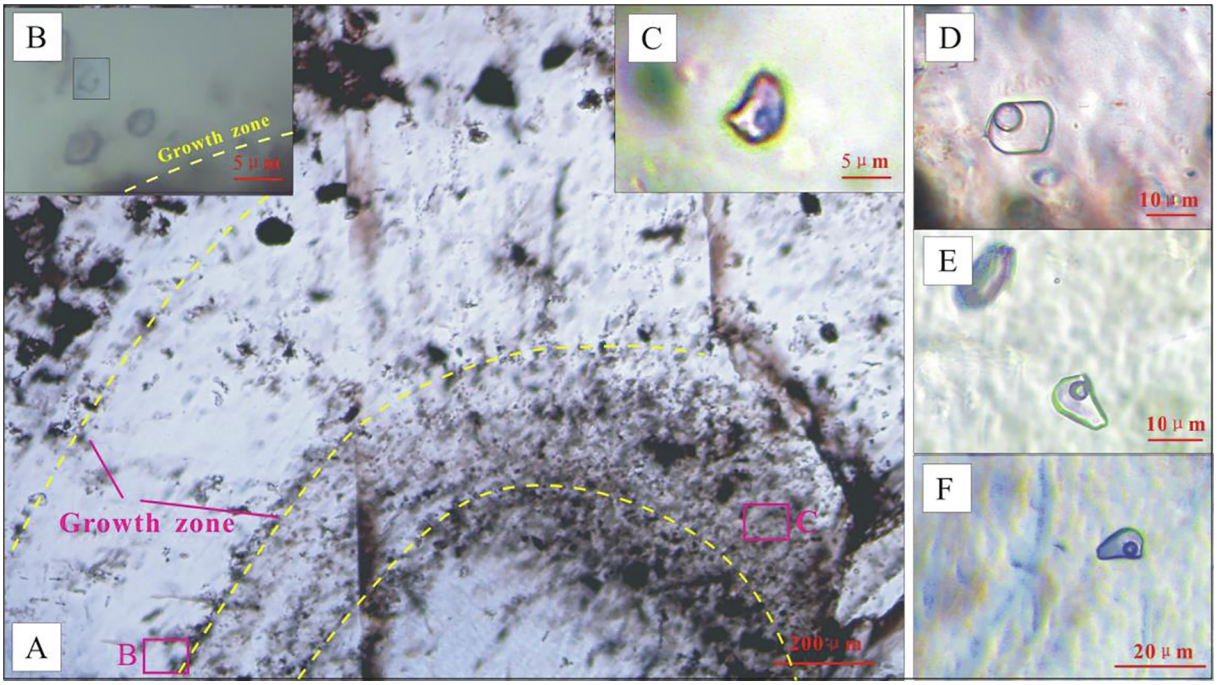

Fig. 12. Photomicrographs of primary fluid inclusions in the Tamusu deposit A) Growth zone in gypsum; B) Gas-liquid inclusion assemblages along growth zone of the gypsum; C) Isolated liquid-vapor inclusion in growth zone of gypsum; D) Isolated fluid inclusions in gypsum; E、F) Fluid inclusions in calcite veins.

Table 3
Summary of microthermometric data and calculated parameters for fluid inclusions from the Tamusu deposit.

Sample no.	Lithology	Mineral	FI types (N)	Size (μm)	Vol(%)	Th (°C)	$T_{m,\ ice}$(°C)	Salinity (wt%)
BF14	red coarse-grained sandstone with vertical gypsum veins	gypsum vein	L-typ(9)	6 to 20	5 to 35	243 to 267	−15.2 to −8.3	12.1 to 18.8
BF15	purplish red medium-grained sandstone with vertical gypsum veins	gypsum vein	L-typ(9)	5to 10	5 to 35	210 to 273	−11.4 to −7.7	11.3 to 15.4
BF07	gray siltstone with vertical gypsum veins	gypsum vein	L-typ(13)	5 to 20	5 to 30	209 to 278	−14.3 to −6.6	10.0 to 18.0
BF09	gray fine-grained mudstone with vertical calcite veins	calcite vein	L-typ(7)	5 to 15	5 to 25	205 to 267	−17.3 to −5.4	17.1 to 20.7

$T_{m,ice}$: temperature of final ice melting; Th: homogenization temperature; L: liquid; V: vapor; Vol = vapor/ (vapor + liquid);(N):number of measured fluid inclusions.

the uranium mineral associations in the high-grade ores indicate that hydrothermal activity played an important role in the uranium enrichment. The Co, Ni, Cu, Y, Bi and Zn contents in the high-grade U-bearing sandstone are much higher than that in the other types of sandstone, but consistent with that of the veins. Cu, Ni, Co and Zn are active elements in medium-low temperature reducing hydrothermal fluids and are rarely enriched at room temperature (Crerar and Barnes, 1976; Seward and Barns, 1997; Simmons et al., 2005; Liam and John, 2017), so it is generally believed that their enrichment is controlled by hydrothermal fluids (Luo et al., 2013; Jin et al., 2015).

The REE patterns and δEu values in the high-grade U-bearing sandstone are consistent with those of the veins, showing LREE-enriched and low δEu characteristics (Fig. 11B), which are similar to those in vein-type U deposits (Mercadier et al., 2011; Frimmel et al., 2014). Weathering and diagenesis have little effect on the redistribution of REEs in a supergene environment unless there is a very high water/rock ratio in clastic rocks (Mclennan and Taylor, 1979; Liu, 1991; Rollison, 1993). In a reducing environment, some Eu^{3+} is converted to Eu^{2+} and separated from the other REEs, producing an δEu anomaly (Zhao and zhou, 1997; Zhu et al.; 2005). This suggests that the high ΣREE and low δEu of the high-grade U ores in the Tamusu deposit were caused by intense water-rock interaction in a reducing hydrothermal environment. EMPA observations indicate chalcopyrite, selenite and other minerals are associated with uranium minerals in the high-grade ores, suggesting a direct relationship between the hydrothermal fluids and the formation of the high-grade uranium ores. However, the EMPA and trace element analysis results show that the uranium mineralization mainly occurs in the sandstone, and is scarce in the hydrothermal veins, which indicates that uranium transported by the hydrothermal fluids is insignificant.

According to previous studies, during the eruption of the Suhongtu Formation basalt, a large number of vertical fissures formed in the upper Bayingobi Formation, which provided a channel for the migration of the deep hydrothermal fluids. Under the influence of the surrounding volcanic events, the formation water in the deep strata gradually migrated upward through fractures to the uranium host sandstone, resulting in large-scale alteration and solidification of the sandstone.

6.3. Mechanisms of uranium precipitation

The acid-base properties of the fluids have a great influence on the migration forms of uranium. Thermodynamic analysis has shown that the most stable form of U(VI) is uranyl carbonate complex in weak alkaline (pH > 8) fluids (Min and Zhang, 1992). Thus, the $[UO_2(CO_3)_2]^{2-}$ complex is inferred to be the main migration form of U (VI) in the oxidation zone of sandstone-type uranium deposits. Many experiments have proved that the solubility of uranyl carbonate complex increases with temperature in alkaline conditions (Wang, 1980; Rao et al., 2003; Chen and Guo, 2007). When the geochemical conditions change from alkaline to acidic, the stability of $[UO_2(CO_3)_2]^{2-}$ is destroyed, resulting in the precipitation of uranium minerals (Wang, 1980). UO^{2+} ions separated from uranyl complexes will be stabilized under reducing conditions as pitchblende (UO_2) (Min and Zhang, 1992). Significant kaolinization is normally found around U-bearing sandstone in sandstone-type uranium deposits, which serves as direct evidence for fluids becoming a weakly acidic environment (Li et al. 2011).

Because of continuous oxidation, the oxidized zone in the Tamusu deposit extends almost throughout the sandstone layer, and non-oxidized regions inside the sandstone are rare. Therefore, the oxidized sandstone is in direct contact with the gray mudstone, without a

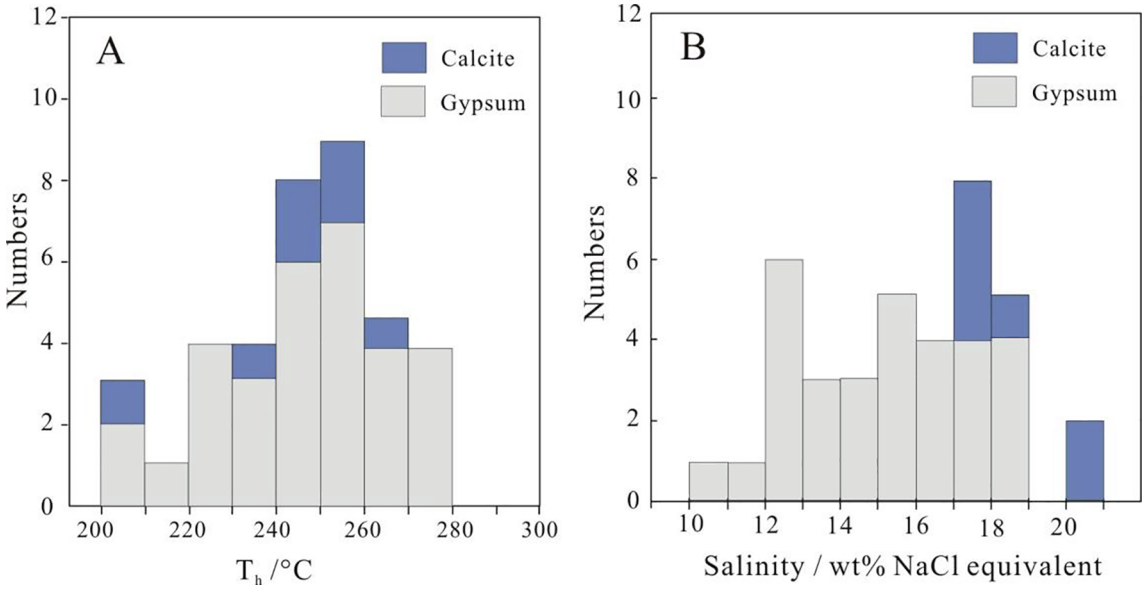

Fig. 13. Histograms of homogenization temperatures (T_h) (A) and salinities for fluid inclusions (B) in veins of the Tamusu deposit.

Table 4
Representative S, C–O isotope concentrations for different types of samples analyzed in the Tamusu deposit (in ppm).

Sample	Mineral	$\delta^{13}C_{PDB}$	$\delta^{18}O_{PDB}$	$\delta^{18}O_{SMOW}$	Sample	Mineral	Depth (m)	$\delta^{34}S_{CDT}$
B38	carbonate cement of gray sandstone	1.8	−11.7	18.8	B30	microcrystal pyrite in gray sandstone or mudstone	−140.5	−24.0
B04		−1.7	−13.0	17.4	B14		−521.3	−29.0
B17		0.9	−11.2	19.3	B11		−545.0	−38.4
B45		−6.8	−11.8	18.7	B08	microcrystal pyrite in U-bearing sandstone	−549.7	−12.2
B32	carbonate cement of red or yellow sandstone	−4.5	−13.2	17.3	BN51		−510.9	−0.3
B77		−0.1	−3.5	27.2	B26	pyrite crystal in veins	−66.0	−5.6
B33		−3.4	−10.6	19.9	B27		−83.5	−5.5
B07		0.5	−14.7	15.7	B28		−118.4	−5.4
B03		−1.1	−10.7	19.8	S01		−453.1	−21.7
B37		−3.0	−7.9	22.7	B22-1		−460.9	−21.9
B25	rock powder of marl	2.8	−6.1	24.6	B15-1		−500.7	−24.5
B63		3.5	−3.2	27.6	B29-1		−577.3	−33.8
B53		0.4	−8.8	21.8	B36		−622.6	−40.1
B55		−1.6	−10.3	20.2	B15-2	gypsum crystal in veins	−500.7	10.0
B40		1.0	−12.1	18.4	S02		−453.1	6.7
B50	calcite crystal of veins	−4.5	−7.7	22.9	B29-2		577.3	−30.0
B28		−2.5	−12.9	17.6	B22-2		460.9	−13.4
B35		−2.0	−11.9	18.6	B34	gypsum cement	−448.6	11.3
B24		−0.4	−17.1	13.2	B13		−509.8	11.4
B38		−1.9	−13.8	16.6	B52		−510.9	11.9

kaolinization sandstone belt. The solubility of $[UO_2(CO_3)_2]^{2-}$ and pitchblende in the alkaline environment increased with temperature, and formed high-concentration zones at the top and bottom of the oxidized sandstone. When the reducing acidic hydrothermal fluids encountered the high-concentration alkaline $[UO_2(CO_3)_2]^{2-}$ zone, a decrease in the pH of the oxidation fluid resulted in decomposition of the uranyl carbonate. U^{6+} was reduced to U^{4+} by S^{2-} and HS^- in the hydrothermal fluids, forming pitchblende and coffinite. The metals carried by the hydrothermal fluids including Ti, Cu and Zn were used to precipitate brannerite and various sulfides including pyrite, galena and selenium minerals.

In summary, oxidizing fluids provided the necessary conditions for uranium migration and were the basis for the formation of the large-scale sandstone-type uranium deposit. The involvement of hydrothermal fluids changed the pH and Eh conditions of the mineralization, superimposed and reformed the low-grade uranium ores formed in the early stage, and formed high-grade uranium ores, with special uranium mineral assemblages and large amounts of metal sulfides. At the same time, hydrothermal fluids caused the general consolidation of the sandstone, terminated the migration of supergene oxidizing fluids in the sandstone pores, and finally fixed the position of the uranium orebodies.

6.4. A metallogenic model for the Tamusu deposit

Based on our studies of the fluid inclusions, isotopes, and geochemistry, we propose a uranium mineralization model for the Tamusu deposit (Fig. 15), which involves four stages. (i) A synsedimentary/early diagenetic stage with trapping of uranium in a wetland reduced environment, during which only a few mudstone-type uranium orebodies were formed. Uranium may have been adsorbed on clay mineral surfaces or reduced by organic matter (Spirakis, 1996; Bonnetti et al., 2015). (ii) A late diagenetic stage with the formation of oxidation zones, during which most of the low-grade U-bearing sandstone was formed. This stage began after the deposition of the upper Bayingobi Formation, resulting in an almost complete oxidation of the sand bodies. Uranium minerals were formed in a redox environment and mainly occur as pitchblende associated with pyrite and organic matter. (iii) A stage of hydrothermal fluid activity with carbonate recrystallization and formation of many new metal minerals, during which most of the high-grade U-bearing ores were formed. The eruption of volcanic rocks at the end of the Early Cretaceous raised the temperature of the Tamusu deposit and formed hydrothermal fluids. The environment of mineralization was changed by the mixing of supergene oxidizing alkaline fluids and the reducing acid hydrothermal fluids.

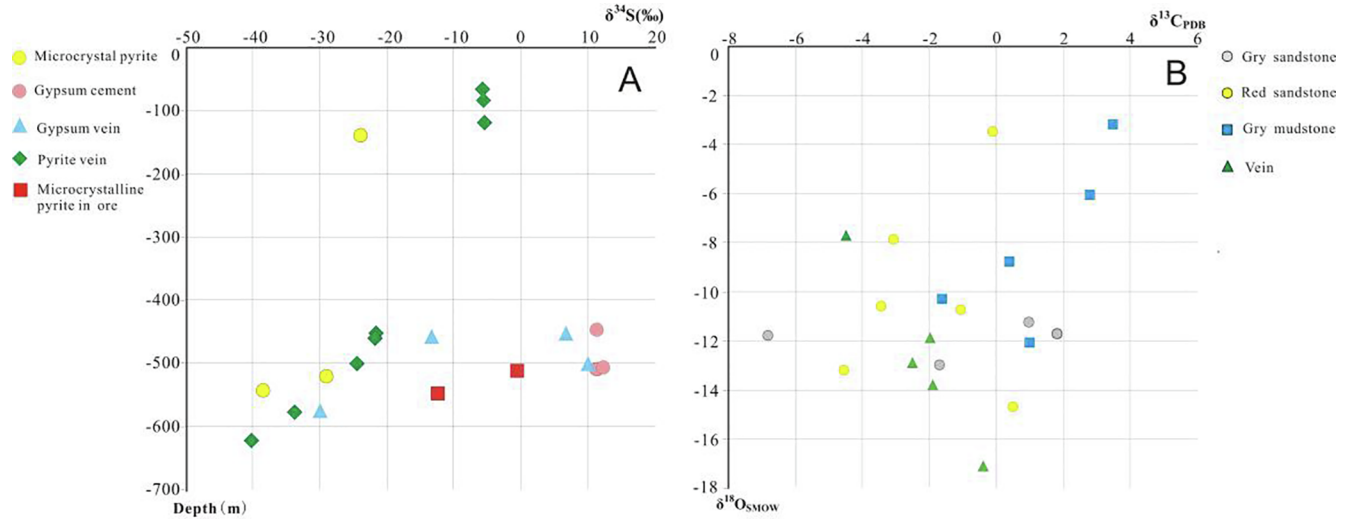

Fig. 14. Characteristics of S isotope (A) and C–O isotope (B) in different samples.

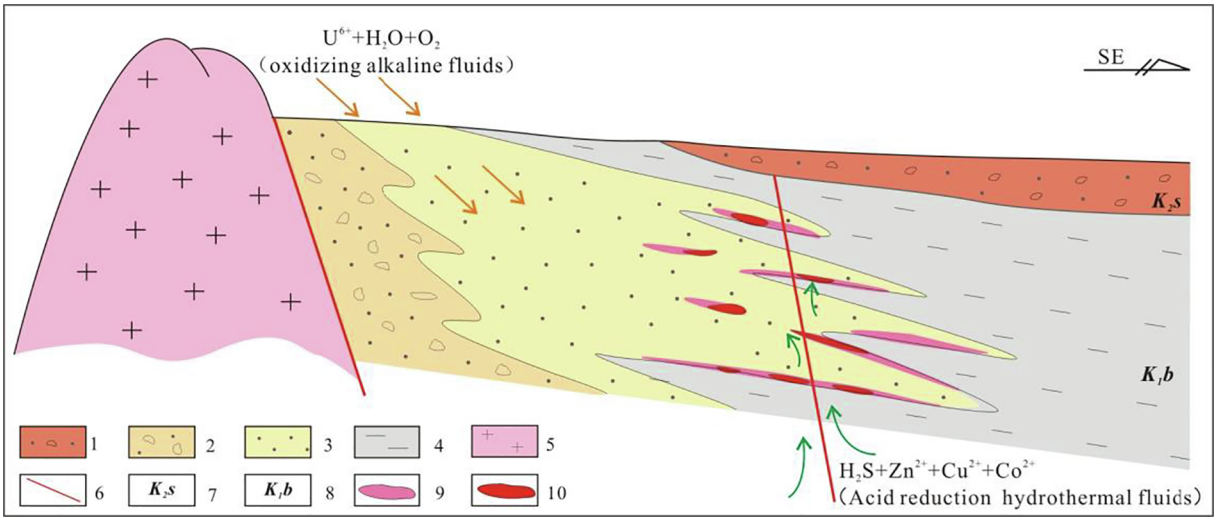

Fig. 15. A genetic model for the Tamusu U deposit. 1) Primary red conglomerate; 2) Sandy conglomerate; 3) Oxidized sandstone; 4) Grey mudstone; 5) Granite; 6) Fault; 7) Wulansuhai Formation of Upper Cretaceous; 8) Bayingobi Formation of Lower Cretaceous; 9) U-bearing sandstone; 10) High grade U-bearing sandstone.

Low-grade uranium ores were superimposed and reformed, and high-grade uranium ores were formed, characterized by coffinite and brannerite associated with metal sulfides. (iv) A late stage of cementation, sealing the mineralization. Field studies show that there are some loose yellow sandstones related to the uranium orebodies near the oxidizing fluids recharge area (Shen et al., 2014). Therefore, it is possible that a minor part of the uranium mineralization was remobilized during this late stage.

6.5. Implications for exploration

This study indicates that hydrothermal overprinting may significantly modify the geology and grade of sandstone-hosted uranium deposits, which has implications for uranium exploration and exploitation. It is therefore important to recognize potential effect of hydrothermal fluids on sandstone-type uranium deposits. Studies on the Tamusu and other deposits suggest that the combination of trace elements, mineral assemblages and uranium mineralogy is a powerful means to identify the relationship between hydrothermal fluids and uranium mineralization (Li et al. 2011; Luo et al., 2012; Zhang, 2016).

Meso-Cenozoic magmatic activity is intensive in the central and eastern basins of northern China, and is consistent with the main uranium mineralization age of some deposits (such as the Qianjiadian uranium deposit, Luo et al., 2012), indicating that hydrothermal fluids may have been involved in the metallogenic processes. Studies of many deposits show that hydrothermal fluids do not provide uranium for sandstone-type uranium deposits, which may be the main reason that there has been little interest in studying hydrothermal overprinting so far. However, uranium metallogenic environment will be changed by the mixture of deep hydrothermal fluids and shallow oxidizing fluids, which may affect the redistribution of uranium. The effect of the change in Eh levels on uranium precipitation has been generally emphasized, while changes in the pH levels are often neglected. Many experiments have confirmed that changes in the pH value are important for decomposition of uranyl carbonate complex and play the same role as Eh under certain conditions (Chen and Guo, 2007; Zhao, 2017). Therefore, we should pay more attention to the effect of hydrothermal overprinting on uranium mineralization, including the effect of pH change, in sedimentary basins.

7. Conclusions

(i) The Tamusu uranium deposit was first formed from interlayer oxidation- reduction processes in sandstone, and modified by hydrothermal fluids.

(ii) Alteration mineral assemblages and fluid inclusions suggest that, hydrothermal fluids are of moderate-high temperature, reducing and acidic. The C–O–S stable isotopes indicate that the hydrothermal fluids may originate mainly from the formation water in the deep strata.

(iii) EMPA and trace element analysis show that there is a direct relationship between hydrothermal fluids and the high-grade ores. The hydrothermal fluids changed the mineralization conditions, overprinted and reworked the low-grade uranium ores, forming high-grade uranium ores.

Acknowledgements

This study was funded by the National Basic Research Program of China (grant No. 2015CB453002), the International Geoscience Comparison Program (IGCP, Grant No. IGCP675) and Fundamental Science on Radioactive Geology and Exploration Technology Laboratory (grant No. RGET1612). The Geological Team No. 208, BOG, CNNC is acknowledged for their help during sampling. We are very grateful to the editors and two anonymous reviewers for their constructive comments and suggestions which improved the paper significantly.

References

Abzalov, M.Z., 2012. Sandstone-hosted uranium deposits amenable for exploitation by in-situ leaching technologies. Appl. Earth Sci. 121, 55–64.
Adams, S.S., 1991. Evolution of genetic concepts for principal types of sandstone uranium deposits in the United States. Econ. Geol. Monogr. 8, 225–248.
Aubakirov, K.B., 2016. A New Interpretation of the Formation of Sandstone type Uranium Deposits. Beijing Research Institute of Uranium Geology, China, pp. 3–35.
Bodnar, R.J., 1993. Revised equation and table for determining the freezing point depression of H_2O-NaCl solutions. Geochim. Cosmochim. Acta 57, 683–684.
Bonhoure, J., Kister, P., Cuney, M., Deloule, E., 2007. Methodology for rare earth element determinations of uranium oxides by ion microprobe. Geostand. Geoanal. Res. 31, 209–225.
Bonnetti, C., Cuney, M., Malartre, F., Michels, R., Liu, X., Peng, Y., 2015. The Nuheting deposit, Erlian Basin, NE China: synsedimentary to diagenetic uranium mineralization. Ore Geol. Rev. 69, 118–139.
Chen, Z., Guo, Q., 2007. Mechanism of U-reduction and concentration by sulphides at sandstone type uranium deposits. Uranium Geol. 23 pp. 321-327 + 334 (in Chinese with English abstract).
Claypool, G.E., Holser, W.T., Kaplan, I.R., Sakai, H., Zak, I., 1980. The age curves of sulfur and oxygen isotopes in marine sulfate and their mutual interpretation. Chem. Geol. 28, 199–260.
Conliffe, J., Azmy, K., Greene, M., 2012. Dolomitization of the Lower Ordovician Catoche

Formation: implications for hydrocarbon exploration in western Newfoundland. Marine Petroleum Geol. 30, 161–173.
Crerar, D.A., Barnes, H., 1976. Ore solution chemistry; V, solubilities of chalcopyrite and chalcocite assemblages in hydrothermal solution at 200 to 350 °C. Econ. Geol. 71, 772.
Cuney, M., Kyser, K., 2008. Recent and not-so-recent developments in uranium deposits and implications for exploration. Min. Assoc. Can. 39, 257.
Curiale, J.A., Bloch, S., Rafalska-Bloch, J., Harrison, W.E., 1983. Petroleum-related origin for uraniferous organic-rich nodules of southwestern. Oklahoma. AAPG Bull. 67, 588–608.
Deng, P., Shu, L.S., Tan, Z.Z., 2003. The Geologic setting for the formation of rich uranium ores in Zhuguang-Guidong large-scale uranium metallogenic area. Geol. Rev. 49, 486–491 (in Chinese with English abstract).
Ding, Y., Hou, S.R., 2012. Characteristics and genesis of uranium deposits in Bayingobi basin. Mineral Deposits 31S, 193–194 (in Chinese with English abstract).
Fan, A.P., Liu, Y.Q., Yang, R.C., Feng, Q., Zhang, F.X., Han, Z., 2007. Study on diagenesis of sandstone type uranium deposits in Dongsheng area of Ordos Basin. Sci. China Earth Sci. 37S, 166–172 (in Chinese with English abstract).
Friedman, I., O'Neil, J.R., 1977. Complication of stable isotope fractionation factors of geochemical interest. Data of geochemistry. US Geol. Surv. Prof, 440–463.
Frimmel, H.E., Schedel, S., Brätz, H., 2014. Uraninite chemistry as forensic tool for provenance analysis. Appl. Geochem. 48, 104–121.
Granger, H.C., Warren, C.G., 1978. Some speculations on the genetic geochemistry and hydrology of roll-type uranium deposits. In: 30th Annual Conference, Wyoming Geological Association Guidebook, pp. 349–361.
Guan, P., Zhang, W.T., Wu, X.S., Xiong, J.Y., 2006. Diagenesis of the Cretaceous Yuyang formation sandstone in Jianghan Basin and its thermodynamic analysis. Acta Petrologica Sinica 22, 2144–2150.
Han, W., 2017. Study of Sedimentary-Tectonic Evolution since Late Paleozoic and its Impacts on Oil and Gas Geological Conditions of Yin-E Basin. PhD Dissertation. Northwestern University, China, pp. 117–120.
Hansley, P.L., Spirakis, C.S., 1992. Organic matter diagenesis as the key to a unifying theory for the genesis of tabular uranium–vanadium deposits in the Morrison Formation, Colorado Plateau. Econ. Geol. 87, 352–365.
Harshman, E.N., 1972. Uranium rolls in the United States. The Mountain Geologist 9, 135–141.
He, Z.B., Luo, Y., Ma, H.F., 2010. Sedimentary facies characteristics of ore-bearing target horizon and its relationship to sandstone-type uranium mineralization in Bayingobi Basin. Uranium Geol. 27, 11–18 (in Chinese with English abstract).
Hoefs, J., 1987. Stable Isotope Geochemistry. Springer-Verlag, Berlin, pp. 208.
Huang, S.J., Tong, H.P., Liu, L.H., Hu, Z.W., Zhang, X.H., Yu, J.L., Huang, K.K., 2009. Petrography, geochemistry and dolomitization mechanisms of Feixianguan dolomites in Triassic, NE Sichuan, China. Acta Petrologica Sinica 25, 2363–2372 (in Chinese with English abstract).
Ingham, E.S., Cook, N.J., Cliff, J., Ciobanu, C.L., Huddleston, A., 2014. A combined chemical, isotopic and microstructural study of pyrite from roll-front uranium deposits, Lak Eyre Basin, South Australia. Geochim. Cosmochim. Acta 125, 440–465.
Jansa, L.F., Noguera Urrea, V.H., 1990. Geology and Diagenetic history of overpressured sandstone reservoirs, Venture Gas Field, Offshore Nova Scotia, Canada. AAPG Bull. 74, 1640–1658.
Jin, L.Y., Qin, K.Z., Li, G.M., Li, Z.Z., Song, G.X., Meng, Z.J., 2015. Trace element distribution in sulfides from the Chalukou porphyry Mo-vein-type Zn-Pb system, northern Great Xing'an range, China: Implications for metal source and ore exploration. Acta Petrologica Sinica 31, 2417–2434.
Li, R.X., Duan, L.Z., Chen, B.Y., Zhang, S.N., 2011. Alteration and metallogeny on the oxic-acid/anoxic-alkali interface of the Dongsheng uranium deposit in northern Ordos basin. Geotectonica et Metallogenia 35, 525–532.
Li, T., 1994. Element abundances of china's continental crust and its sedimentary layer and upper continental crust. Geochimica 2, 140–145 (in Chinese with English abstract).
Liam, A.B., John, P., 2017. Selenium and molybdenum enrichment in uranium roll-front deposits of Wyoming and Colorado, USA. J. Geochem. Explor. 180, 101–112.
Lin, S.X., Gong, X.F., Zhang, T.S., 2017. Deep geofluid and uranium metallogenesis in Meso-Cenozoic basins. Uranium Geol. 33, 321–328 (in Chinese with English abstract).
Liu, C.Y., Qiu, X.W., Wu, B.L., Zhao, H.G., 2007. The basic characteristics of the metallogenic domain of the Middle East Asian energy mineral resources and the dynamic environment for its formation. Sci. China Earth Sci. 37S, 1–15 (in Chinese with English abstract).
Liu, W.J., 1991. Application of commonly used data in sedimentary geochemistry. Shanxi Geol. 6, 109–123 (in Chinese with English abstract).
Luo, C., Xu, Y.K., Cheng, F.G., Zhang, C.J., Ni, S.J., Tang, C.Y., Liang, J., Zhang, C.J., 2013. The trace element geochemical characteristics and genesis analysis of the 373 uranium deposits in Guangxi. Acta Geol. Sin. 87, 715–729.
Luo, Y., He, Z.B., Ma, H.F., Sun, X., 2012. Metallogenic characteristics of Qianjiadian sandstone uranium deposit in Songliao basin. Mineral Deposits 31, 391–400 (in Chinese with English abstract).
Mclennan, S.M., Taylor, S.R., 1979. Rare earth element mobility associated with uranium mineralisation. Nature 282, 247–250.
Meng, Q.R., Hu, J.M., Yuan, X.J., Jin, J.Q., 2002. Structure, evolution and origin of Late Mesozoic extensional basins in the China-Mongolia border region. Geol. Bull. China 21, 224–231 (in Chinese with English abstract).
Mercadier, J., Cuney, M., Lach, P., Boiron, M.C., Bonhoure, J., Richard, A., Leisen, M., Kister, P., 2011. Origin of uranium deposits revealed by their rare earth element signature. Terra Nova 23, 264–269.
Min, M.Z., Xu, H.F., Chen, J., Fayek, M., 2005. Evidence of uranium biomineralization in sandstone-hosted roll-front uranium deposits, northwestern China. Ore Geol. Rev. 26, 198–206.
Min, M.Z., Zhang, F., 1992. Genesis of Uranium Mineralogy. Atomic Energy Press, Beijing, pp. 54–120.
Nie, F.J., Yan, Z.B., Xia, F., Li, M.G., Lu, Y.Y., Cai, J.F., Guo, F.N., Ning, J., 2017. Hot fluid flows in the sandstone-type uranium deposit in the Kailu basin, Northeast China. Geol. Bull. China 36, 1850–1866 (in Chinese with English abstract).
Ohmoto, H., 1986. Stable isotope geochemistry of ore deposits. Rev. Mineral. Geochem. 16, 491–559.
Ohmoto, H., Goldhaber, M.A., 1997. Sulfur end carbon isotopes. In: Barnes, H.L. (Ed.), Geochemistry of Hydrothermal Ore Deposits, 3th Edition. John Wiley & Sons, New York, pp. 517–611.
Pan, J.Y., Liu, C.D., Guo, G.L., Chen, A.P., Chen, F.Z., Yan, Z.B., Chen, Y.P., Wu, R.G., 2009. The discovery of selenium-bearing minerals in the Tamusu sandstone-type uranium deposits, Inner Mongolia, China and its significance. Acta Mineralogica Sinica 29, 44–48 (in Chinese with English abstract).
Penney, R., 2012. Australian sandstone-hosted uranium deposits. Appl. Earth Sci. 121, 65–75.
Rao, L., Garnov, A.Y., Jiang, J., Di Bernardo, P., Zanonato, P., Bismondo, A., 2003. Complexation of uranium (VI) and samarium (III) with oxydiacetic acid: temperature effect and coordination modes. Inorganic Chem. 42, 3685–3692.
Reynolds, R.L., Goldhaber, M.B., 1982. Biogenic and nonbiogenic ore-forming processes in the South Texas uranium district: evidence from panna Maria deposit. Econ. Geol. 77, 541–556.
Rollison, H.R., 1993. Using Geochemical Date: Evaluation, Presentations. Interpretation. Pearson Education Limited, Zimbabwe, pp. 106–111.
Seward, T.M., Barns, H.L., 1997. Metal transport by hydrothermal ore fluids. In: Barnes, H.L. (Ed.), The Geochemistry of Hydrothermal Ore Deposits, third ed. John Wiley and Sons Inc., New York, pp. 435–486.
Shen, K.F., Yang, J.X., Hou, S.R., Dai, M.J., Li, H.J., 2014. Uranium prospecting breakthrough, achievement expanding and prospecting orientation in main Mesozoic-Cenozoic sedimentary uranium basins of Inner Mongolia. China Geol. 41, 1304–1313 (in Chinese with English abstract).
Sheppard, S.M.F., 1986. Characterization and isotopic variations in natural waters. Rev. Mineral. 16, 165–183.
Simmons, S.F., White, N.C., John, D.A., 2005. Geological characteristics of epithermal precious and base metal deposits. In: Economic Geology 100th Anniversary Volume, pp. 485–522.
Spirakis, C.S., 1996. The roles of organic matter in the formation of uranium deposits in sedimentary rocks. Ore Geol. Rev. 11, 53–69.
Suess, E., Whiticar, M.J., 1989. Methane-derived CO_2 in pore fluids expelled from the Oregon subduction zone. Palaeogeogr. Palaeoclimatol. Palaeoecol. 71, 119–136.
Sun, S.S., McDonough, W.F., 1989. Chemical and isotopic systematics of oceanic basalts, implication for mantle composition and processes. In: Saunders, A.D., Norry, M.J. (Eds.), Magmatism in the Ocean Basins. Geological Society of London, pp. 313–345.
Taylor, B.E., 1986. Magmatic volatiles: Isotope variation of C, H and S reviews in mineralogy. Mineral. Soc. Am. 16, 185–226.
Taylor, S.R., Mclennan, S.M., 1985. The Continental Crust: Its Composition and Evolution. Mlackwell, Oxford, pp. 9–56.
Wang, F.F., Liu, C.Y., Qiu, X.W., Guo, P., Zhang, S.H., Cheng, X.H., 2017. Characteristics and distribution of world's identified sandstone-type uranium resources. Acta Geol. Sin. 91, 2021–2046 (in Chinese with English abstract).
Wang, J.F., 1980. Migration precipitation and metallogenic model of uranium in hydrothermalism. J. East China Univ. Technol. 2, 184–200 (in Chinese).
Wang, Z.Q., Cao, S.L., Pan, J.Y., Guan, T.Y., Zhang, G.Y., 2005. Trace element geochemistry of No. 511 uranium ore deposit in Xinjiang. Mineral. Deposits 24, 409–415 (in Chinese with English abstract).
Wei, P.S., Zhang, H.Q., Chen, Q.L., 2006. Petroleum Geologic Feature and Exploration Prospect of the Inggen-Ejin Basin. Petroleum Industry Press, Beijing, pp. 24–48.
Wei, W., Zhu, X.M., Guo, D.B., Fei, L.Y., Su, H., Jiang, F.H., 2015. Carbonate cements in Lower Cretaceous Bayingebi sandstone reservoirs in Chagan sag, Yin-e Basin: formation phases and formation mechanisms. Geochemistry 44, 590–599 (in Chinese with English abstract).
Worden, R.H., Morad, S., 2003. Clay minerals in sandstones: controls on formation, distribution and evolution. In: Worden, R.H., Morad, S. (Eds.), Clay Mineral Cements in Sandstones. International Association of Sedimentologists Special Publication, pp. 1–41.
Wu, B., Wei, A., Liu, C., Song, Z., Hu, L., Wang, D., Cun, X., Sun, L., Luo, J., 2015. Stable isotope tracing on the formation of white sandstone in Yan'an group, northern Ordos basin, and its geological significance. Earth Sci. Front. 22, 205–214 (in Chinese with English abstract).
Wu, R.G., Zhou, W.P., Liu, P.H., Hou, S.R., Wang, Y., Ma, F., Pan, J., 2008. Analysis of metallogenic condition and prospecting potential of sandstone type uranium deposit in Tamusu district of Bayinggebi basin. Uranium Geol. 24, 4–31 (in Chinese with English abstract).
Wu, R.G., Zhou, W.P., Xu, Z., Liu, P.H., Zhang, L., 2010. Discussion on the chronology of Suhongtu formation in Bayingebi basin. Uranium Geol. 26, 152–157 (in Chinese with English abstract).
Wulser, P.-A., Brugger, J., Foden, J., Pfeiffer, H.-R., 2011. The sandstone-hosted Beverley uranium deposit, Lake Frome basin, south Australia: mineralogy, geochemistry and time-constrained model for its genesis. Econ. Geol. 106, 835–867.
Yang, X.Y., Ling, M.X., Sun, W.D., Lai, X.D., Liu, C.Y., Miao, J.Y., Sun, W., 2009. The genesis of sandstone type uranium deposits in the Ordos Basin, NW China: constraints provided by fluid inclusions and stable isotopes. Int. Geol. Rev. 51, 422–455.
Zhang, C.Y., Nie, F.J., Hou, S.R., Deng, W., Wang, J.L., Zhang, L., 2015. Study on hydrothermal alteration and relation with uranium mineralization of the Tamusu

exogenetic uranium deposit, Inner Mongolia, China. Acta Mineralogica Sinica 35, 79–86 (in Chinese with English abstract).
Zhang, J.D., 2016. Innovation and development of metallogenic theory for sandstone type uranium deposit in China. Uranium Geol. 32, 321–332 (in Chinese with English abstract).
Zhang, L., Liu, C.Y., Mostafa, F., Wu, B.L., Lei, K., Cun, X.N., Sun, L., 2017. The nuheting deposit, Erlian Basin, NE China: synsedimentary to diagenetic uranium mineralization. Ore Geol. Rev. 69, 118–139.
Zhao, F.M., 2017. Recognition on the role of reducing action in uranium metallization. Uranium Geol. 33 pp. 193-198 + 214 (in Chinese with English abstract).
Zhao, F.M., Zheng, Z.X., 1983. Classification and genesis of mineral associations in hydrothermal uranium deposits of China. Geol Rev. 29, 220–226.
Zhao, Z.H., Zhou, L.D., 1997. REE geochemistry of some alkali-rich intrusive rocks in China. Sci. China Earth Sci. 20, 145–158.
Zheng, Y.F., 1999. Oxygen isotope fractionation in carbonate and sulfate minerals. Geochem. J. 33, 109–126.
Zhong, F.P., Zhong, J.H., Wang, Y., You, W.F., 2014. Geochemistry characteristics and origin of Early Cretaceous volcanic rocks in Suhongtu depression, Inner Mongolia, China. Acta Mieralogica Sinica 34, 107–116.
Zhu, B.Q., Cheng, Z.D., Ying, F.X., 1996. Relation of organic acid generated by kerogen to secondary porosity of reservoir. Exp. Pet. Geol. 18, 206–215 (in Chinese with English abstract).
Zhu, X.Y., Wang, Y.L., Wang, Z.C., Zhang, C.J., Liu, J.H., 2005. Application of REE characteristics in the study of sandstone type uranium deposit: a case study of a uranium deposit in the northern Sichuan Basin. Geol Rev. 51, 401–408 (in Chinese with English abstract).